THE BELL SYSTEM
TECHNICAL JOURNAL

DEVOTED TO THE SCIENTIFIC AND ENGINEERING
ASPECTS OF ELECTRICAL COMMUNICATION

Volume 55 October 1976 Number 8

Basic Fluid-Dynamic Considerations in the Drawing of Optical Fibers

By F. T. GEYLING

(Manuscript received January 9, 1976)

The optical fiber drawing process is considered in its totality—from source to forming zone to draw-down region and take-up end—as a problem in fluid dynamics. Fiber drawing of most glasses is dominated by viscous stresses, surface tension effects, and quenching rates. This contrasts with the drawing of textile fibers, where other fluid properties and non-Newtonian effects can play important roles. Preliminary time-invariant "base flow" models are developed for glass drawing, using the one-dimensional, small-slope approximation of extensional flow. First-order sensitivities of these base flows to changes in operating conditions are examined via a stability analysis. Two important instability mechanisms, denoted as the tensile and capillary modes of dynamic fiber response, are discussed. Several follow-on objectives arising from this study are described.

I. INTRODUCTION

Stringent tolerances set on optical fibers used in communication systems have generated a need for understanding the fluid dynamics of the fiber drawing process. The responses of this process to various disturbances, especially those resulting in perturbations of the fiber diameter, are of interest.

For steady-state drawing, one seeks analytic models that interrelate the draw-down ratio, draw force, flow rate, and some characteristic temperature. Such models serve two purposes: they predict the effects of changes in the operating parameters and can therefore be used in the control of industrial drawing processes; they also provide a "base

state" for the theoretical study of dynamic responses. Such responses could be due to a variety of physical disturbances; for example, mechanical vibrations, thermal transients, ambient gas flow, and even acoustic noise. All of these disturbances may produce variations in the diameter of the finished fiber.

In studying the perturbations of liquid fibers, our philosophy departs somewhat from the more traditional one of stability analysis in textile engineering. Textile fiber studies, in general, strive to avoid fiber rupture and gross distortions of the thread line. (See, for example, Refs. 1 through 9.) In cases where continuous drawing of textile fibers is impossible, much emphasis is placed on the prediction and control of thread length, i.e., the filament lengths attainable between spontaneous ruptures.

The drawing of optical fibers takes filament continuity for granted. However, the ultimate optical application is sensitive to small diametral perturbations, far from rupture. Moreover, optical fibers are usually drawn at higher viscosities and draw forces than textile fibers. Starting from a much higher melt temperature, the subsequent viscosity increase due to quenching of the glass is much more severe than in polymers. Also, in its molten state glass is more nearly Newtonian than most polymers.

Our purpose, then, is to model the mechanisms by which perturbations arise in the glass-drawing process and are frozen into the finished fibers. Based on this understanding, we hope to control fiber dimensions within the tolerances imposed by optical considerations (e.g. Ref. 10).

The fluid dynamics of fiber forming involve a source flow, also referred to as the forming zone, and a draw-down region. The forming zone is usually characterized by a rapidly contracting flow issuing from the bottom of a preform, or pulled from an orifice at the bottom of a crucible (Fig. 1a). In drawing from preforms, we may distinguish between a very sharply contracting configuration (Fig. 1b), commonly encountered with laser heating, and a more gradual contraction that results from furnace heating (Fig. 1c). We include in Fig. 1d the case of an overheated preform, where the forming zone consists essentially of a liquid drop from which the filament is drawn. The different forming-zone configurations shown in Fig. 1 can imply fundamental differences in the flow field, as far as the steady-state and potential instabilities are concerned. For example, there is some evidence[11] to suggest that the overheated preform, Fig. 1d, is capable of self-sustained oscillations at critical draw speeds, whereas, at noncritical speeds, the liquid reservoir in the pendant drop tends to absorb perturbations coming from the take-up end.

The forming zone makes a continuous transition to the draw-down

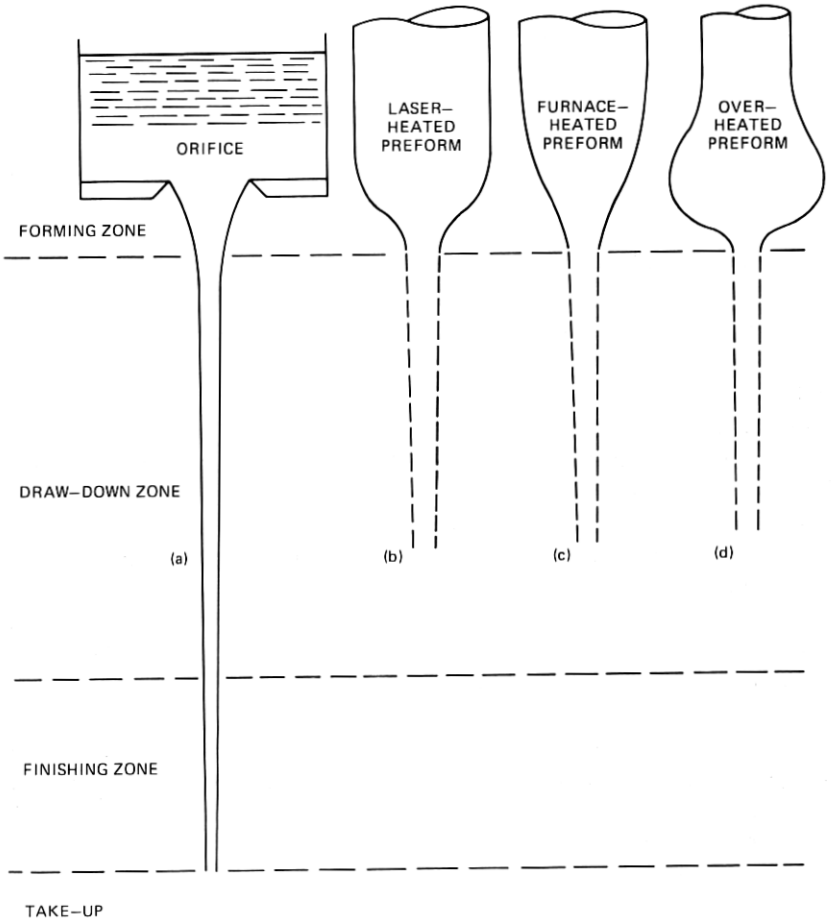

Fig. 1—Fiber-drawing methods.

region, where an essential part of the fiber contraction occurs. Typical draw-down ratios, defined as terminal velocity/source velocity, in this region run between 10 and 100. Most fiber stability studies place major emphasis on the draw-down region, because of its physical importance and mathematical tractability. However, the role of incipient perturbations in the forming zone cannot be ignored. The essential need for modeling this part of the flow field, if only by numerical simulations, is obvious. For completeness, we also recognize that a very small amount of fiber deformation occurs beyond the draw-down region; but this falls within the visco-elastic rather than the fluid-dynamic regime.

Much of the empirical evidence in textile and glass-fiber drawing[1] suggests that fluid dynamics in the draw-down region is governed by

the so-called Trouton viscosity, a measure of the ability of fluid filaments to sustain tensile stress as a function of elongational strain rate. Indeed, if fiber breakage occurs in the draw-down region, it exhibits the neck-down and cohesive separation reminiscent of tensile test specimens. Much of the early modeling by Ziabicki[12,13] and subsequent efforts by Pearson,[5,14] Kasé,[6,7] and others are based on this notion, and for this reason we refer to these analyses as "tensile" models.

In parallel, and possibly quite independent of the tensile mechanism, local flow conditions may exist where surface-tension-driven phenomena play a significant role. Such "capillary" responses could occur at the hot tip of the forming zone, where the viscosity is still quite low and the filament begins to take shape. Capillary models of filament response go back to Rayleigh's classical work,[15,16] with subsequent extensions and experimental corroboration by, for example, Taylor,[9] Tomotika,[17,18] and Weber.[19]

The present paper serves several purposes: (*i*) it generates preliminary base-flow models for the draw-down region, using the one-dimensional, small-slope approximation of elongational flow; (*ii*) it makes a preliminary assessment of sensitivities, through differences in base flow, to changes in operating conditions, such as take-up speed and quenching profile; (*iii*) it presents the tensile and capillary models of dynamic fiber response as fundamentally distinct mechanisms; it explores their applicability to different parts of the draw process by suitable modifications and extensions of existing theories; (*iv*) it projects several follow-on efforts aimed at unified models of the steady and perturbed drawing process, viz. more realistic base-flow models, including heat transfer and two-dimensionality at the start of the draw-down region, and transient-response models, which account for these refinements in the base flow together with possible interactions between capillary and tensile mechanisms.

II. REVIEW OF EARLIER WORK

In this section, we discuss some of the literature on tensile and capillary stability analyses of liquid filaments. Table I relates several key publications and identifies their underlying assumptions and physical models.

The first comprehensive study of tensile fiber models was undertaken by Ziabicki et al.[1–4,12,13,20] Motivated by the textile engineers' interest in potential instabilities and fracture mechanisms, the authors reviewed existing phenomenological evidence on filament "spinning."* They

* This traditional terminology, which suggests twisting a fibrous material into strands, will be avoided henceforth as inappropriate to the drawing of liquid filaments.

Table 1 — Overview of tensile and capillary fiber models

Tensile models, physical features discussed.	Viscosity = 3 μ, inertia, surface tension, quenching, finite draw-down.	Viscosity = 3 μ, stability analyses.	Viscosity = 3 μ, stability experiments.
Pertinent literature	Refs. 1–4, 12, 13, 20: analysis and experimental corroboration of relevant physical factors in base state and some dynamic perturbations.	Refs. 5, 14: dynamic analysis of attenuating fibers, including the effects of viscosity perturbations and different base states.	Refs. 6, 7, 21, 22, 25: experiments corroborating cyclic and transient responses of tensile fiber models.
Capillary models, physical features investigated.	Newtonian viscosity and surface tension.	Inertia and surface tension.	Newtonian viscosity, inertia, and surface tension.
Pertinent literature	Ref. 16: cylindrical filaments neglecting inertia. Refs. 17, 18: adaptation to contracting flows and quenching effects.	Refs. 16, 19: theory of inviscid capillary fluid cylinders.	Refs. 16, 17, 18, 19: complete theories of capillary jets. Modification for quenching effects given here.
	Note: Numerous authors have conducted experiments over the years to demonstrate instabilities of capillary jets and filaments under isothermal, i.e., constant viscosity, conditions.		

also cite experimental evidence that when a filament is formed, say in the wake of a free-falling viscous drop, either a tensile ("cohesive") fracture or capillary separation may sever the flow.

In Ref. 12, a suitable tensile theory is developed for the prediction of finite filament lengths, assuming the cross-sectional distribution of longitudinal velocities to be uniform and the steady-state flow to contract with small slope. Reference 20 accomplishes the same for capillary effects by an adaptation of Rayleigh's classical theory (as we have done independently for our own purposes). Ziabicki's subsequent publications include a thorough evaluation of experimental results, corroborating his predictions of filament lengths.*

Ziabicki's comprehensive effort was followed by a series of papers by Pearson and others, aimed predominantly at tensile stability models. Starting from the simplest possible representation[14]—an isothermal filament under constant viscous tension—progressively more elaborate results were achieved by adding fiber quenching, inertia, surface tension, and gravity. A physical interpretation of this work, however, is difficult since the explicit features of diametral perturbation profiles along the fiber, their time dependence, and their sensitivity to properties of the base state seem poorly understood. We will return to this in Section VII. Ziabicki's tensile flow models and the draw-resonances

* Like other Western readers, the author has been somewhat late in fully recognizing the significance of Ziabicki's work, much of which was initially recorded in Polish journals. Note, however, Ref. 4 for a more recent, comprehensive account.

predicted by Pearson et al. were corroborated by several experimenters. We cite the work of Kasé[21,22] and Donnelly and Weinberger[25] as examples in this area.

As mentioned earlier, the study of surface-tension-driven perturbations contributes another, as yet separate, view of fiber stability which goes back to Rayleigh's classical work as presented in Refs. 15 and 16. Rayleigh himself studied several simplified cases: (*i*) constant viscosity plus surface tension (no inertia), (*ii*) inertia plus surface tension (no viscosity), and (*iii*) constant viscosity plus inertia plus surface tension. Each analysis yields an exact solution of the hydrodynamic perturbation equations for an incompressible liquid contained by a cylindrical boundary with surface tension. Simplifying assumptions are made only in solving the characteristic equations.

Weber[19] showed that exact solutions of the characteristic equation differ little from Rayleigh's approximation. He also considered the effect of aerodynamic drag on the perturbed filament. Tomotika[17,18] extended Rayleigh's model to allow for an ambient viscous fluid that surrounds the filament and is subjected to a steady elongational flow.

For our own purposes, we need to modify Rayleigh's and Tomotika's work to reflect not only contraction in the base flow but also the viscosity buildup due to quenching. These are essential features of such "capillary" models of fiber drawing and are therefore listed explicitly in Table I. A display of diametral response profiles along the fiber and their dependence on wavelength and base-flow properties is given for comparison with tensile stability models.

III. FUNDAMENTAL EQUATIONS AND THE ASSUMPTION OF ONE-DIMENSIONAL FLOW

Let z = axial coordinate
r = radial coordinate
v = axial velocity component
u = radial velocity component
ρ = fluid density, assumed constant
σ = surface tension,
μ = Newtonian viscosity, a function of temperature.

In the cylindrical coordinate system (r, z), the Eulerian equations of mass and momentum conservation read:

$$v_z + u_r + \frac{u}{r} = 0 \tag{1}$$

$$\rho[u_t + uu_r + vu_z] = \frac{\partial \tau_r}{\partial r} + \frac{1}{r}\tau_r + \frac{\partial \tau_{rz}}{\partial z} - \frac{1}{r}\tau_\theta \tag{2}$$

$$\rho[v_t + uv_r + vv_z] = \frac{\partial \tau_z}{\partial z} + \frac{\partial \tau_{rz}}{\partial r} + \frac{1}{r}\tau_{rz}, \tag{3}$$

where τ_r, τ_z, τ_{rz} denote stress components. In all other instances, the subscripts r, z, t denote partial derivatives.

The constitutive relations for an incompressible Newtonian fluid are

$$\begin{aligned} \tau_z &= -p + 2\mu \frac{\partial v}{\partial z} \\ \tau_r &= -p + 2\mu \frac{\partial u}{\partial r} \\ \tau_\theta &= -p + 2\mu \frac{u}{r} \\ \tau_{rz} &= \mu\left(\frac{\partial v}{\partial r} + \frac{\partial u}{\partial z}\right), \end{aligned} \tag{4}$$

where p is the pressure. It is one of the dependent variables, along with u, v, and the free surface configuration $r = a(z, t)$. Equations (1) to (3) have the following boundary conditions:

At $z = 0$:

$$\begin{aligned} v(r, 0, t) &= v_0(r, t) \\ u(r, 0, t) &= u_0(r, t) \\ a(0, t) &= a_0(t). \end{aligned} \tag{5}$$

At $z = L$, the take-up position:

$$v(r, L, t) = v_L(r, t). \tag{6}$$

At $r = a(z, t)$: the kinematic condition

$$v = u\frac{\partial a}{\partial z} + \frac{\partial a}{\partial t} \tag{7}$$

together with tangential and normal surface-stress conditions, which we do not reproduce in detail at this point. (See Appendix A.) Once a solution of this boundary value problem has been found, the draw force at any cross-section follows from

$$P(z, t) = 2a\pi\sigma/[1 + (\partial a/\partial z)^2]^{\frac{1}{2}} + 2\pi \int_0^a r\tau_z dr. \tag{8}$$

In particular, $\Delta P(t) = P(L, t) - P(0, t)$ and, to the extent that the solution for τ_z contains μ, ρ, σ, the expression for ΔP depends on these fluid properties.

The complete set of governing equations for the fiber drawing process includes an energy equation from which the temperature dis-

tribution $T(r, z, t)$ in the draw-down region is determined. This, in turn, yields μ as function of position and time. Strictly speaking, therefore, the heat-transfer equation is coupled to the fluid-dynamic equations. However, since we give it a separate, detailed treatment elsewhere, we uncouple it from this preliminary discussion and introduce $\mu(r, z)$, for nonisothermal draw-down, as a function presumed obtainable from some heat transfer model.

The general axisymmetric, free-surface flow problem posed by (1) to (7) is a formidable one. However, for the purposes of an engineering analysis and to gain some basic insight, much headway can be made by taking advantage of the fact that $|a_z| = 0(\epsilon) \ll 1$ and $|u/v| = 0(\epsilon) \ll 1$ throughout the draw-down region. This "small slope" assumption expresses the obvious fact that fluid flow in fiber drawing is essentially one-dimensional. The consequences of this kinematic feature are developed in Appendix A, taking advantage of the fact that we are dealing with low-Reynolds-number flow away from regions of strong relaxation in velocity profile. Specifically, we find:

(*i*) $v_r \equiv 0$, i.e., "plug" flow throughout the draw-down region.

(*ii*) $\tau_{rz} \propto \epsilon(\tau_z, \tau_r, \tau_\theta)r/a$

(*iii*) $u \propto \epsilon v r/a$

(*iv*) $\tau_r = \tau_\theta$, uniform over the cross-section

(*v*) $\tau_z = -\sigma/a + 3\mu v_z$, over the cross-section,
where 3 μ is the so-called "Trouton" viscosity for extensional flow in a liquid filament.

These features of one-dimensional flow in the draw-down region suggest that mass and momentum conservation may be expressed conveniently in terms of cross-sectional fluxes and stress integrals. Equations of this kind may be obtained formally by integrating over the fiber cross-section: eq. (1) for volume conservation and eq. (3) for the axial momentum balance. Alternatively, we may derive these equations directly by taking a segment, of length dz, from the tapered axisymmetric filament as control volume. We obtain for volume conservation

$$(a^2v)_z + (a^2)_t = 0 \tag{9}$$

and for axial momentum conservation

$$\rho(a^2v^2)_z + \rho(a^2v)_t - 3(a^2\mu v_z)_z - \sigma a_z = 0. \tag{10}$$

For an eventual comparison with the early work of Pearson et al., we also record (10) after the terms in ρ and σ have been dropped. We have the simplified momentum equation

$$a^2\mu v_z = M(t), \tag{11}$$

where M is an arbitrary time function. This equation merely states that the draw force is uniform along the fiber and varies only with t.

For later reference, the time-independent (i.e., steady-state) versions of (9) and (10) yield

$$a^2v = \text{const.} = Q \tag{12}$$

and

$$C = 3a^2\mu v_z - \rho Q v + a\sigma, \tag{13}$$

where C is a constant of integration, viz. the cross-sectional draw force reduced by the momentum flux.

IV. STEADY-STATE SOLUTIONS FOR THE DRAWING PROCESS

In this section, we consider solutions of the time-independent equations (12) and (13). These constitute steady-state representations of the drawing process which are of interest for two reasons. First, they model the steady drawing operation and yield some insight into its controlling parameters, i.e., the dependence of draw force and draw-down profile on the draw-down ratio, the viscosity profile, fluid inertia, and surface tension. Second, they provide reference states on which to build dynamic response models for fiber-stability studies. In this context, such solutions are often referred to as base flow models.

It is well-known in fluid-dynamic stability theory that detailed features of the underlying base flow can be quite important to the predicted dynamic response. Hence, it is necessary that we examine several base-flow solutions of the drawing process for the physical features they represent.

Starting from (13), one observes that the first term on the right-hand side represents the viscous stress effect, the second fluid inertia, and the third a contribution from surface tension. We assume the following fiber dimensions and fluid properties at the start of draw-down:

$$\begin{aligned}
v &= 10 \text{ cm/s} \\
a &= 10^{-2} \text{ cm} \\
v_z &= 100/\text{s (e.g., } \Delta v = 100 \text{ cm/s, over } \Delta z = 1 \text{ cm)} \\
\rho &= 2.5 \text{ gm/cm}^3 \\
\sigma &= 200 \text{ dyn/cm} \\
\mu &= 100 \text{ poise for soda lime glass} \\
&= 1000 \text{ poise for fused silica.}
\end{aligned}$$

Note that the temperature at the interface between forming and draw-down zone is very dependent on as yet unknown fluid-dynamic and heat-transfer conditions in the forming zone. Therefore, the assumed values for μ are rather tenuous. 100 poise probably represents a mini-

mum for soda lime glass, as might be expected in fiber drawing from crucibles.

Given these data, the order-of-magnitude relations between terms in (13) are:

	Viscosity μ (poise)	Viscous stress $3\mu a^2 v'$ (dyn)	Inertia $\rho Q v$ (dyn)	Surface Tension σa (dyn)
Soda lime glass	100	3	2.5×10^{-2}	2
Fused silica	1000	30	2.5×10^{-2}	2

Thus, inertia effects amount to barely 1 percent of the viscous term under the most favorable circumstances, while surface tension can be important when μ is near its minimum. However, physical evidence suggests rapid quenching of glass fibers in the draw-down region. Hence, inertia and surface tension effects soon become negligible as the temperature drops by several hundred degrees over the first few millimeters of the draw-down region, causing μ to grow by several orders of magnitude (see, for example, Ref. 23).

Disregarding, for a moment, the quenching effect that actually occurs in the draw-down region, we briefly consider an isothermal base state for two reasons. First, it permits an understanding of secondary physical effects such as inertia and surface tension, without being obscured by viscosity changes. Second, in later dynamic response studies, the isothermal base state serves as a basis of comparison for the stabilizing effect of the quenching that does occur.

Letting the fluid properties in (13) be independent of z, we consider flow conditions such that inertia and surface-tension effects can be viewed as perturbations in relation to the viscous stress. Eliminating the radius a from (12) and (13) and nondimensionalizing according to

$$\Psi = v/v_0, \qquad \zeta = z/L, \qquad (\ )' = \frac{\partial(\ )}{\partial \zeta},$$

we find

$$\Psi' - D\Psi = -We\Psi^{\frac{1}{2}} + Re\Psi^2, \tag{14}$$

where $v_0 = v$ at $z = 0$, L = length of draw-down region, and $D = LC/3a_0^2 v_0^2 \mu_0$, the nondimensionalized equivalent of C in (13). The inertia and the surface-tension terms are characterized by a Reynolds number $Re = v_0 L\rho/3\mu_0$ and a Weber number, $We = \sigma L/3a_0 v_0 \mu_0$. The elementary solution for (14) with $We = Re = 0$ is

$$\Psi_{(0)} = e^{\zeta \ln E}, \tag{15}$$

where we have used the boundary conditions

$$\Psi = 1 \quad \text{at} \quad \zeta = 0$$
$$\Psi = E \quad \text{at} \quad \zeta = 1$$

and $E = v_L/v_0$ is the so-called "draw-down ratio." Note that $D = \ln E$.

Corrections to this simple base-state solution for small We and Re can be found by perturbation methods. A first-order approximation for $We \ll D$ and $Re \ll D$ is found by substituting (15) into the r.h.s. of (14):

$$\Psi_{(1)} = \exp\left[lnE\zeta + \frac{2We}{lnE}\,(e^{-(lnE/2)\zeta} - 1) + \frac{Re}{lnE}\,(e^{\zeta lnE} - 1)\right]. \quad (16)$$

Resubstituting this into the right side of (14) for a second iteration, terms such as $\exp[e^{\zeta lnE}]$, were approximated by power series prior to quadrature with respect to ζ. Then,

$$\Psi_{(2)} = e^{\zeta lnE}\left\{1 - We\mathfrak{IC}\left[\frac{Re}{2lnE}, \frac{We}{lnE}, -\frac{lnE}{2}, -\frac{(We + \frac{1}{2}Re)}{lnE}, \zeta\right]\right.$$
$$\left. + Re\mathfrak{IC}\left[\frac{2Re}{lnE}, \frac{4We}{lnE}, lnE, -\frac{(4We + \frac{1}{2}Re)}{lnE}, \zeta\right]\right\}, \quad (17)$$

where the expression for $\mathfrak{IC}[a, b, c, d, \zeta]$ is recorded in Appendix B. Numerical results from (17) are best presented in terms of the non-dimensional radius $a/a_0 = \chi$. According to (12)

$$\chi = \Psi^{-\frac{1}{2}}. \quad (18)$$

This has been plotted in Figs. 2 and 3 for a range of values in We and

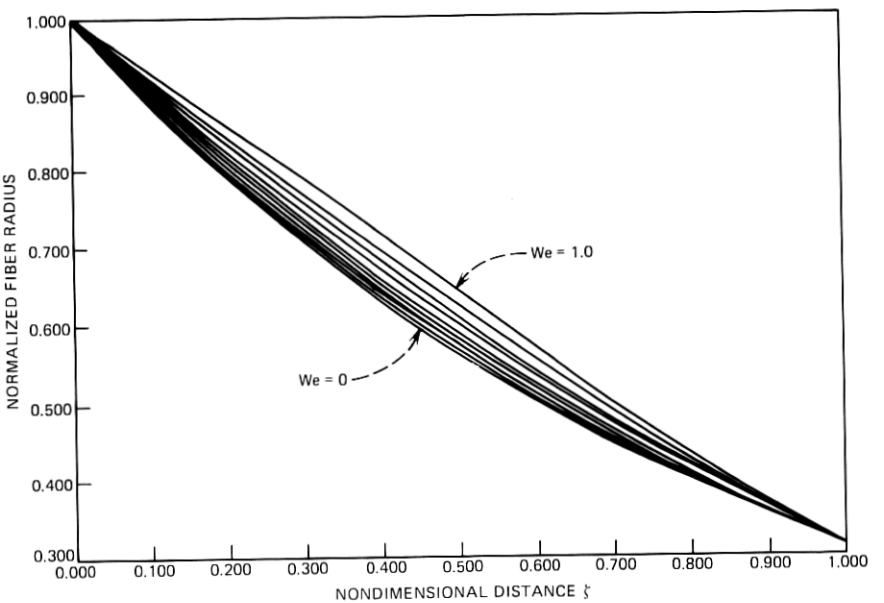

Fig. 2—Perturbation solutions for base-flow profiles with increasing surface tension; $E = 10$, $Re = 0$.

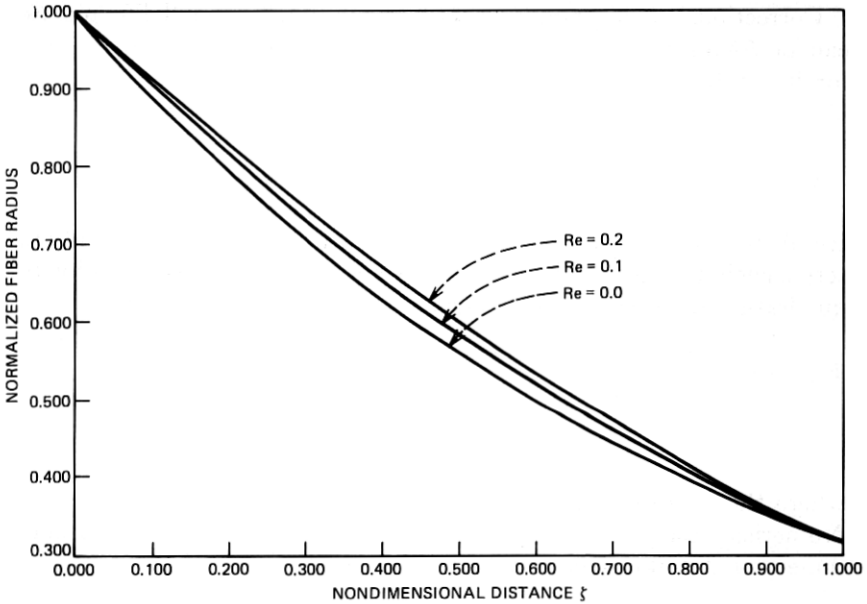

Fig. 3—Perturbation solutions for base-flow profiles with increasing fluid inertia; $E = 10$, $We = 0$.

Re. These results show a tendency for filament contraction to be delayed with increasing surface tension and fluid inertia, a familiar phenomenon from more accurate base-flow models obtained by numerical methods.[24]

Now let us return to the more realistic case of variable viscosity. We denote it $\mu_0\eta(\zeta)$, where the second factor represents only the dimensionless dependence on ζ, with $\eta(0) = 1$. Then (14) becomes

$$\eta\Psi' - D\Psi = -We\Psi^{\frac{1}{2}} + Re\Psi^2. \tag{19}$$

Using an inverse approach, we can, for example, assume $Re \neq 0$, $We = D = 0$ (where $D = lnE$ is no longer true) and $\Psi = e^{\zeta lnE}$, as in (15). This yields

$$\eta = \frac{Re}{lnE} e^{\zeta lnE} \tag{20}$$

and constitutes an inertia-dominated base flow. Experimental data suggest that something like an exponential viscosity buildup along the draw-down region is a fair representation of quenching effects. Note that for this base-flow model,

$$\chi = e^{-(lnE/2)\zeta}, \tag{21}$$

which has the disadvantage that $\chi \to 0$ for $\zeta \gg 1$. To provide a finite

asymptotic value for χ, we may assume a draw-down profile of the form $\chi = fe^{-\alpha\zeta} + g$ with $f + g = 1$, $0 < f, g < 1$, and solve for Ψ from (18) and η from (19).

We summarize the three elementary base-flow models obtained so far with the notation $lnE/2 = \alpha$:

Unquenched base flow; $Re = We = 0$:

$$\chi = e^{-\alpha\zeta}, \qquad \Psi = e^{2\alpha\zeta}, \qquad \eta \equiv 1. \tag{22}$$

Quenched base flow; $Re \neq 0$; $We = 0$;

$$\begin{aligned} &\chi \to 0 \quad \text{for} \quad \zeta \to \infty : \\ &\chi = e^{-\alpha\zeta}, \qquad \Psi = e^{2\alpha\zeta}, \qquad \eta = e^{2\alpha\zeta}. \end{aligned} \tag{23}$$

Quenched base flow; $Re \neq 0$; $We = 0$;

$$\chi \text{ finite for } \zeta \to \infty :$$

$$\chi = (fe^{-\alpha\zeta} + g), \quad \Psi = 1/(fe^{-\alpha\zeta} + g)^2, \quad \eta = e^{\alpha\zeta}/(fe^{-\alpha\zeta} + g). \tag{24}$$

In addition to the inertia-dominated base flows (23) and (24), we can show that

$$\chi = fe^{-\alpha\zeta} + g, \qquad \Psi = \frac{1}{g^2}\left(1 - 2\frac{f}{g}e^{-\alpha\zeta}\right), \qquad \eta = \frac{1}{g}e^{\alpha\zeta} \tag{25}$$

is a solution of the approximate fluid-dynamic and heat-transfer equations, for small α, if we let $Re = We = 0$ and assume

$$\mu = \mu_0 e^{\beta(1 - T/T_0)},$$

where T_0 is the initial temperature and $\beta \gg 1$. This represents a quenched base flow that is not inertia-dominated, in keeping with some of the perturbation equations discussed later on. Note that for each of these base-flow models $\partial a/\partial z = 0(\alpha a_0/L)$. Since $\alpha = 0(1)$ but $a_0/L \ll 1$, this means that $|\partial a/\partial z| \ll 1$ and confirms the basic assumption providing for one-dimensional flow, as discussed in Section III. Note also that the viscosity profiles in models (23), (24), and (25), which reflect a cooling process along the fiber, are connected with the draw-down profile through the parameter α. This parameter is indicative of the quenching rate in η, and also controls χ', the slope of the draw-down profile.

The draw-force follows from any of these solutions by the obvious relation, in dimensional form,

$$P = \pi a^2 \tau_z + 2a\pi\sigma = 3\pi a^2 \mu v_z + \pi a\sigma. \tag{26}$$

If we neglect σ and substitute one of the base flows, we find that P

depends on a_0, v_0, μ_0 as well as the draw-down ratio and the quenching rate α; all of which could be expected on physical grounds.

Clearly, we could refine upon the viscosity profiles to be used in simple base-flow models. Since some experimental temperature profiles tend to show an exponential decay and the viscosity temperature relation for many glasses is of the form $\eta \sim e^{k/T}$, we might consider functions of the form

$$\eta = r + s \exp(e^{2\alpha t}).$$

However, such elaborations result in a loss of mathematical simplicity and usually lead to equations for Ψ that require numerical integration. At that point, it seems more appropriate to solve the coupled heat-transfer/flow problem by numerical means. This has been done and is documented elsewhere.[24]

V. PERTURBATION EQUATIONS FOR TENSILE STABILITY MODELS

In this section, we develop the first-order perturbation equations necessary for a linear stability analysis of tensile fiber models. Let the first-order solution of (9), (10), and (11) be denoted

$$\begin{aligned} \bar{a} &= a(z)[1 + \hat{a}(z, t)] \\ \bar{v} &= v(z)[1 + \hat{v}(z, t)] \\ \bar{\nu} &= \nu(z)[1 + \hat{\nu}(z, t)], \end{aligned} \tag{27}$$

where $a(z)$, $v(z)$, and $\nu(z)$ represent radius, velocity, and kinematic viscosity for a suitable base state, in dimensional form for the time being, and $\hat{a}$, $\hat{v}$, $\hat{\nu}$ are dimensionless first-order perturbations of these quantities.

Substituting (27) into (9), the first-order variation of the continuity equation reads

$$\hat{a}_z + \frac{1}{v}\hat{a}_t + \frac{1}{2}\hat{v}_z = 0. \tag{28}$$

Similarly, (10) without the surface-tension term becomes

$$\begin{aligned} \hat{v}_{zz} + \hat{v}_z\left(\frac{\nu_z}{\nu} + \frac{v_z}{v} - \frac{2v}{3\nu}\right) - \frac{1}{3\nu}\hat{v}_t + \hat{a}_z\left(\frac{2v_z}{v} - \frac{2v}{3\nu}\right) \\ - \frac{2}{3\nu}\hat{a}_t + \hat{a}\left(2\nu\frac{v_z}{v} - \frac{2v}{3}\right)_z\Big/\nu + \hat{v}\left(\frac{\nu v_z}{v} - \frac{2v}{3}\right)_z\Big/\nu \\ = -\hat{\nu}_z\frac{v_z}{v} - \hat{\nu}\left(\frac{\nu v_z}{v}\right)_z\Big/\nu \end{aligned} \tag{29}$$

and from (11), the momentum equation without inertia terms,

$$2\hat{a} + \hat{\nu} + \hat{v} + \frac{v}{v_z}\hat{v}_z = \frac{d(t)}{P_0}, \tag{30}$$

where we have used $a^2\nu v_z = P_0 = \text{const.}$ from (11) and $d(t)$ is a perturbation of $M(t)$. Since the examples in later sections use the base states of Section IV, it is convenient to nondimensionalize the space and time variables as

$$\alpha\zeta = \vartheta \qquad \frac{v_0\alpha t}{L} = \tau \tag{31}$$

and use the notation

$$\frac{d(\ )}{d\vartheta} = (\ )' \quad \text{and} \quad \frac{d(\ )}{d\tau} = (\ )\cdot. \tag{32}$$

The specific versions of (28), (29), and (30) now develop as follows. With the base states (22) or (23), eq. (28) becomes

$$\hat{a}' + \tfrac{1}{2}\hat{v}' + \dot{a}e^{-2\vartheta} = 0. \tag{33}$$

Neglecting inertia in the momentum equation, (22) and (30), for the unquenched inertialess base state, yields

$$2\hat{a} + \hat{v} + \hat{p} + \tfrac{1}{2}\hat{v}' = \varphi(\tau), \tag{34}$$

where φ is an arbitrary function of τ. On the other hand, the momentum equation (29), using the quenched inertia-dominated base state (23) leads to

$$\hat{v}'' - 4\hat{v} - 4\dot{a}e^{-2\vartheta} - 2\dot{v}e^{-2\vartheta} = -2\hat{p}' - 4\hat{p}. \tag{35}$$

Turning now to the inertialess, quenched base state (25), we revert to (28) and (30) as basic equations, but reserve the substitution of v and v_z from (25) for a later time.

For some of the examples treated in later sections, it is convenient to eliminate $\hat{v}$ from (34) and (35) by means of (33) and similarly from (28) and (30) for base state (25). The resulting equations for $\hat{a}$ are recorded in Appendix C for later reference.

Conversely, the boundary conditions for some problems demand an equation in $\hat{v}$. This is the case with steady-state responses to changes in the takeup velocity, which we treat in the next section. If (27) is used in (12) and we let $\bar{Q} = Q(1 + \hat{q})$, the first-order variation of that equation yields

$$2\hat{a} + \hat{v} = \hat{q}. \tag{36}$$

Next, consider (13), where we neglect surface tension and perturbations in ν. As noted before, the constant C may be interpreted as a force parameter, carried from the forming zone to the draw-down region. Taking the first variation of (13), letting $\bar{C} = C(1 + \hat{c})$, and eliminating $\hat{a}$ by means of (36),

$$\hat{v}_z - \frac{v}{3\nu}\hat{v} = -\frac{C}{3Q\nu}\hat{c} + \hat{q}\left(\frac{v}{3\nu} - \frac{v_z}{v}\right). \tag{37}$$

Nondimensionalizing the base-flow variables in this equation according to Section IV, we have

$$\hat{v}_\zeta - \frac{Re\Psi}{\eta}\hat{v} = \frac{k}{\eta} + \left(\frac{Re\Psi}{\eta} - \frac{\Psi_\zeta}{\Psi}\right)\hat{q}, \tag{38}$$

where

$$k = \frac{LC\hat{c}}{3a_0^2 v_0 \mu_0}.$$

Equation (38) is designed to yield changes in the steady-state velocity profile, $\hat{v}$, as a function of $\hat{q}$ and k, which are perturbations of the volume flux and force parameter of the base flow.

In summary, this section has developed first-order perturbation equations based on the continuity and momentum equations of Section III. The perturbation equations were given in terms of $\hat{a}$ or $\hat{v}$ as needed for the steady-state and dynamic-response studies to be pursued in Sections VI and VII.

VI. PERTURBATIONS OF THE BASE FLOW

In this section, we use the time-independent versions of perturbation equations derived in Section V to display changes in several base-flow solutions due to shifts in such steady-state parameters as the boundary values and the viscosity profile along the fiber. Since these parameters are often accessible to control in real fiber-drawing processes, their effects on the steady flow are of operational interest. Obviously such effects could be determined by differencing neighboring base-flow solutions in the control-parameters space; however, exhibiting the changes (analytically) as first-order perturbations can yield useful insight for the design of feedback controls.

We start by examining the response of steady state (24) to a change $\hat{v}_L$ in take-up speed. Substituting the appropriate base-flow expressions for Ψ and η into (38), one has

$$\hat{v}' - Re\frac{e^{-\vartheta}}{\chi}\hat{v} = ke^{-\vartheta}\chi + (Re - 2f)\frac{e^{-\vartheta}}{\chi}\hat{q}, \tag{39}$$

where

$$\vartheta = \alpha\zeta \qquad (\ )' = \frac{\partial(\ )}{\partial\vartheta} \qquad s = fe^{-\vartheta} + g$$

and a factor of $1/\alpha$ has been absorbed in Re and k. The boundary condition for (39) is

$$\hat{v} = \hat{v}_L \quad \text{at} \quad \vartheta = \vartheta_L = \alpha. \tag{40}$$

We find

$$\hat{v} = V\chi^{-Re/f} - \frac{k\chi^2}{2(1+f)} + \left(\frac{2f}{Re} - 1\right)\hat{q} \tag{41}$$

with

$$V = \left[\hat{v}_L + \left(1 + \frac{2f}{Re}\right)\hat{q}\right]\chi_L^{Re/f} + \frac{k\chi_L}{2(1+f)}\,(2 + Re/f),$$

where $\chi_L = \chi(z_L)$. Given (41), the corresponding changes in fiber radius $\hat{a}$ follow from (36).

Additional features of interest with (41) are $\hat{v}$ at $z = 0$ and perturbations of the draw force at either end. Thus,

$$\hat{v}_0 = \hat{v}(0) = V - \frac{k}{2(1+f)} + \left(\frac{2f}{Re} - 1\right)\hat{q}. \tag{42}$$

For the draw force,

$$\bar{P} = P(1 + \hat{p}) = 3\pi\mu\bar{a}^2\bar{v}_z,$$

which yields

$$\hat{p} = \hat{q} + \frac{v}{v'}\hat{v}' = \hat{q} + \frac{e^{\vartheta}s\hat{v}'}{2f}.$$

From this,

$$\hat{p}_0 = \hat{q} + \frac{VRe}{2f} + \frac{k}{2(1+f)} \tag{43}$$

and

$$\hat{p}_L = \hat{q} + \frac{VRe}{2f}\chi_L^{-Re/f} + \frac{k\chi_L^2}{2(1+f)}, \tag{44}$$

the changes in draw force, as function of $\hat{v}_L$, $\hat{q}$, and k.

The solution (41) is of little more than conceptual value as long as $\hat{q}$ and k are unknown. Recall from (38) that these parameters represent perturbations in the integration constants of the base-flow solution for the draw-down region: $\hat{q}$, a change in the volume flux, and k, a change in the force parameter of the momentum equation. Such changes must, in general, be expected to enter from the forming zone when the steady state is altered due to $\hat{v}_L$.

Fortunately, $\hat{q} = 0$ for drawing from a preform that is fed at a constant rate. However, the exit flow from a crucible (Fig. 1a) does not provide such a simple condition. If operating at a low head in the reservoir, we would expect the entrance flow into the orifice to be affected by changes in the take-up speed. In neither case does there exist an obvious condition for the force parameter k [i.e., $\hat{c}$ and C, see eq. (38)].

A theory of the forming zone should be able to relate $\hat{v}_0$ and $\hat{p}_0$ on the one hand with $\hat{q}$ and k on the other. Given such relations, these would combine with (42) and (43) to determine $\hat{q}$ and k in terms of $\hat{v}_L$, and hence $\hat{v}$, $\hat{a}$, $\hat{p}$ as functions of $\hat{v}_L$. Depending on the different situations depicted in Fig. 1, the relations of $\hat{v}_0$, $\hat{p}_0$ vs $\hat{q}$, k in the forming zone could vary considerably. In some cases, an understanding of the complex fluid-dynamic and heat-transfer processes of the forming

zone (see Fig. 1d) would seem essential for a satisfactory representation of speed-diameter-force relations at the take-up end.

In the remainder of this section, we examine the sensitivity of steady-state flow in the draw-down region to changes in the viscosity profile. Such changes can be viewed as consequences of perturbations in the heat-transfer mechanism. Our primary purpose is to determine response amplitudes for $\hat{a}$, the perturbation in draw-down profile, as functions of $\hat{\nu}_0$, an amplitude parameter of the viscosity perturbation. Once again we encounter the problem of assuming reasonable boundary conditions at $z = 0$ without a dynamic model of the forming zone.

We consider two different cases: the draw-down response without inertia effects imposed on the unquenched, inertialess base state (22), and the response with inertia effects imposed on the quenched, inertia-dominated base state (23). In particular, we shall be working with eqs. (76) and (77) after deletion of the time derivatives.

In both cases, we consider a viscosity perturbation of the form

$$\hat{\nu} = \hat{\nu}_0 \vartheta e^{-\gamma \vartheta}, \tag{45a}$$

which represents a distribution of arbitrary amplitude and spread, determined by $\hat{\nu}_0$ and γ, respectively. A family of such functions is displayed in Fig. 4 for $1 \leqq \gamma \leqq 6$. Note that for a given value of γ

$$\frac{\nu}{\hat{\nu}_{0_{max}}} = \frac{1}{\gamma e}, \tag{45b}$$

the peak viscosity perturbation, normalized w.r.t. $\hat{\nu}_0$.

Let us consider various boundary conditions that may be applicable to solutions of this problem. If we assume that the fiber is drawn from a preform with constant feed and take-up conditions, an obvious boundary condition is

$$\hat{a}(\vartheta_L) = 0. \tag{46a}$$

In view of $\hat{q} \equiv 0$, it seems reasonable to assume that the forming zone will respond with $\hat{p}(0) = 0$. $\hat{v}'(0)$ can be eliminated from these two conditions to yield

$$a'(0) - \frac{a'(0)}{a(0)} \hat{a}(0) = 0. \tag{46b}$$

If three boundary conditions are needed, we take

$$\hat{a}(0) = 0, \tag{46c}$$

and then, according to (46b), also $\hat{a}'(0) = 0$. Finally, for a fourth condition, let

$$\hat{a}'(\vartheta_L) = 0, \tag{46d}$$

which implies that $p(\vartheta_L) = 0$, i.e., no perturbation of the draw force

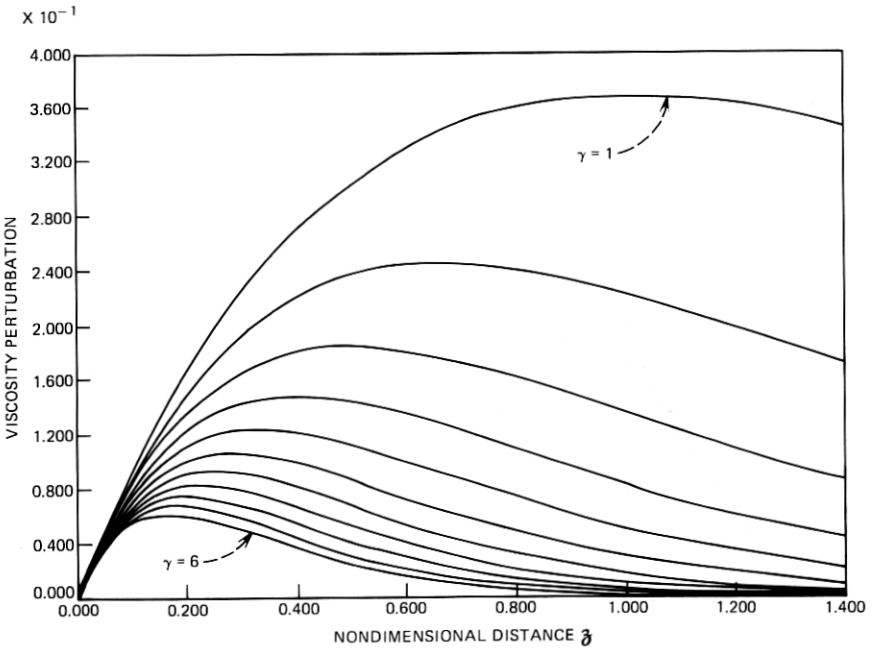

Fig. 4—Profiles of the viscosity perturbation, $\nu/\nu_0 = \partial e^{-\gamma\partial}$.

occurs at the take-up end. Conditions (46) will be invoked as necessary with increasing order of the perturbation equations.

We start by considering the inertialess perturbation eq. (77). We have

$$\hat{a} = -\frac{\hat{p}_0}{\gamma} e^{-\gamma\partial}\left(\frac{1}{\gamma} + \partial\right) + B_1\partial + B_2. \tag{47}$$

Results from (47) have been plotted in Fig. 5 to represent the effect of viscosity perturbations on the unquenched base state. Note the non-monotonic evolution of these curves with increasing γ.

Next, we examine the corresponding results, including effects of fluid inertia. Integrating (76) after deletion of the time derivatives, the quenched inertia-dominated base state (23) leads to

$$\hat{a}''' + 2\hat{a}'' - 4\hat{a}' - 8\hat{a} = \hat{p}'' + 4\hat{p}' + 4\hat{p} + C. \tag{48}$$

C is a constant of integration.

Substituting (45) into (48), we obtain

$$\hat{a}(z) = \frac{-\hat{p}_0}{(\gamma+2)}\left(\partial + \frac{1}{\gamma+2}\right)e^{-\gamma\partial} + B_1 e^{2\partial} + (B_2 + B_3\partial)e^{-2\partial} + B_4. \tag{49}$$

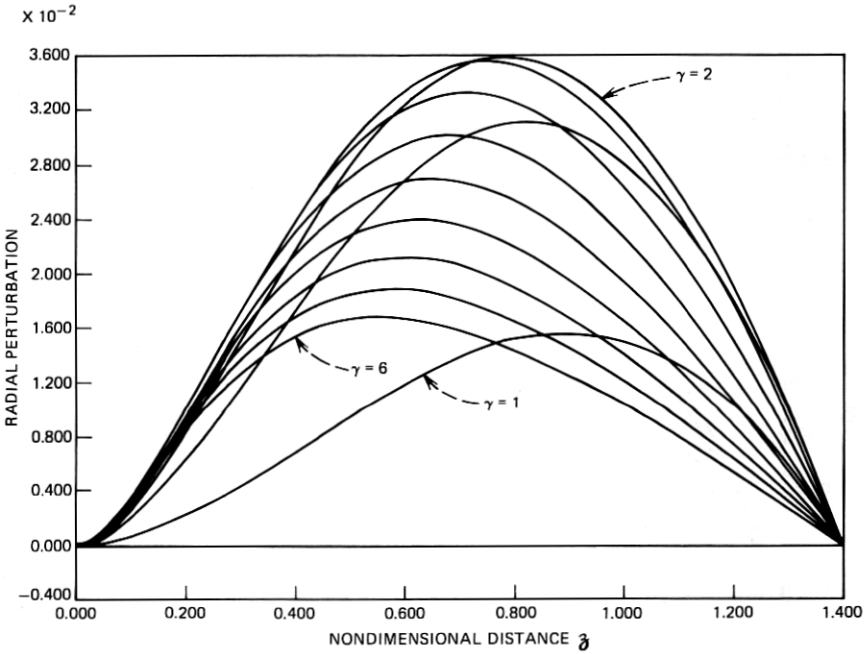

Fig. 5—Draw-down response to the viscosity perturbations of Fig. 4, without fluid inertia, for unquenched base flow.

Figure 6 shows (49), the effect of viscosity perturbations on the quenched, inertia-dominated base state, over the range $1 \leqq \gamma \leqq 6$. Note that the presence of quenching significantly alters the evolution of response curves in Fig. 6, which becomes monotonic with γ. Typical amplitudes in this case are about one-half to one-third as large as for the unquenched base flow (Fig. 5).

The main inference to be drawn from a comparison of Figs. 5 and 6 is that typical peak amplitudes for $\hat{a}/\hat{v}_0$ are reduced significantly due to fluid inertia and quenching.

By way of specific example, we consider results for $\gamma = 3.5$:

Maximum for viscosity perturbation (Fig. 4)	$\hat{v}/\hat{v}_0 = 0.110$
Maximum for response without inertia on unquenched base state (Fig. 5)	$\hat{a}/\hat{v}_0 = 0.018$
Maximum for response with inertia on quenched base state (Fig. 6)	$\hat{a}/\hat{v}_0 = 0.005$

The latter case, which represents the more realistic model, also predicts the lower response amplitudes. Thus, for example, a 10-percent departure from the nominal viscosity profile would cause only a 0.5-percent departure from the draw-down profile.

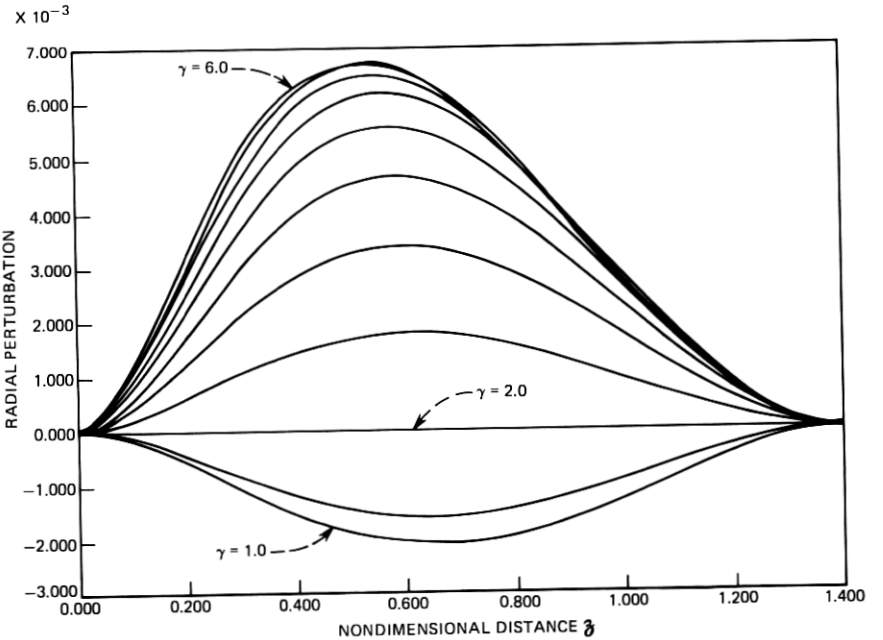

Fig. 6—Draw-down response to viscosity perturbations, with fluid inertia, for quenched base flow.

In summary, the first-order results given in this section yield a qualitative indication of base flow responses to time-invariant changes of the boundary conditions and of the viscosity profile. As stated in Section IV, a more satisfactory treatment of viscosity effects may be achieved by numerical integration of the base-flow equations, which introduce heat-transfer perturbations through the energy equation. However, the question of realistic interface conditions between the drawn-down region and forming zone remains open until the latter is included in our model.

VII. THE DYNAMIC RESPONSE OF TENSILE FIBER MODELS

We turn now to the dynamic response of tensile fiber models for the unquenched and quenched base flows; i.e., we address solutions of the equations in Appendix C, including the time-dependent terms. Unfortunately, the formulation allowing for fluid inertia, eq. (76), does not lend itself to a simple solution. We therefore seek what preliminary insight can be gained from solutions obtainable with (77) and (78), i.e., by neglecting inertia in the perturbation equations.

Starting with (77), which represents perturbations of the unquenched base flow, the operator on the left-hand-side suggests a gen-

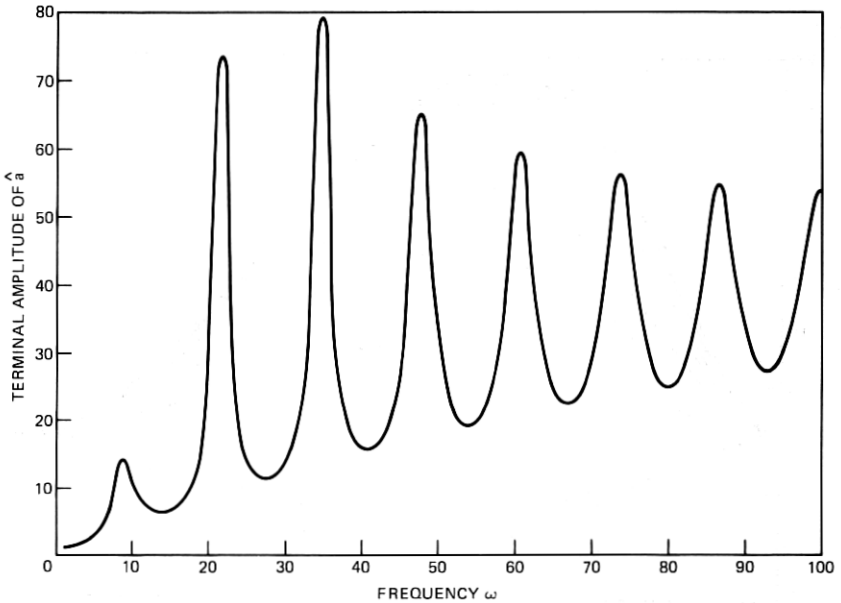

Fig. 7—Tensile fiber model: frequency response of surface perturbation at $\vartheta_L = 2$ for base state [eq. (22)].

eral solution of traveling waveform

$$\hat{a}' = f(\tau + \tfrac{1}{2}e^{-2\vartheta}) \tag{50}$$

and

$$\hat{a}_c = \int f(\tau + \tfrac{1}{2}e^{-2\vartheta})d\vartheta + \Phi(\tau), \tag{51}$$

where $\Phi(\tau)$ is an arbitrary time function. This solution may be used to represent radial excitations at the source or take-up end or to satisfy boundary conditions in the presence of a particular solution. In the former case, where $\hat{a}(0, \tau) = \sin \omega\tau$, we reconstruct a solution by Pearson and Matovitch[14] of the form

$$\hat{a}(\vartheta, \tau) = A_1(\vartheta) \sin \omega\tau + A_2(\vartheta) \cos \omega\tau \tag{52}$$

with the terminal response amplitude

$$A(\omega, \vartheta_L) = [A_1^2(\omega, \vartheta_L) + A_2^2(\omega, \vartheta_L)]^{\frac{1}{2}}. \tag{53}$$

This is normalized with respect to $\hat{a}_0$, the amplitude of radial perturbations at $\vartheta = 0$, and plotted, for later comparison, in Fig. 7 as a function of ω, for $\vartheta_L = 2$. It shows a series of response peaks presumably due to the absence of quenching from the base state (22), used in (77).

These response peaks are commonly referred to in the literature as

"draw resonances." The author takes exception to this term since it implies the existence of natural frequencies contingent on the interaction of system inertia and some restoring force, neither of which is obvious in the present model. Nevertheless, experimental evidence confirms the occurrence of highly amplified responses near some of the "critical" frequencies predicted by Pearson's model. Typical radial perturbation profiles for $\hat{a}(\vartheta, \tau)$ are shown in Fig. 8 for $\omega = 100$, at $T = 0$, the start of a period, and $T = 0.25$, its quarter-point. They illustrate the spatial amplification of surface perturbations occurring along the draw path.

Since the direct physical realization of radial perturbations at $\vartheta = 0$ may be difficult, we now examine the effect of viscosity perturbations that are convected along the fiber as a consequence of fluctuations in the heat source; i.e.,

$$\hat{\nu} = g(\tau + \tfrac{1}{2}e^{-2\vartheta}). \tag{54}$$

Substitution into (77) yields the inhomogeneous equation

$$\left(\frac{\partial}{\partial \tau} + e^{2\vartheta}\frac{\partial}{\partial \vartheta}\right)\hat{a}' = -\dot{g}(\tau + \tfrac{1}{2}e^{-2\vartheta}), \tag{55}$$

where the dot is also used to designate differentiation with respect to

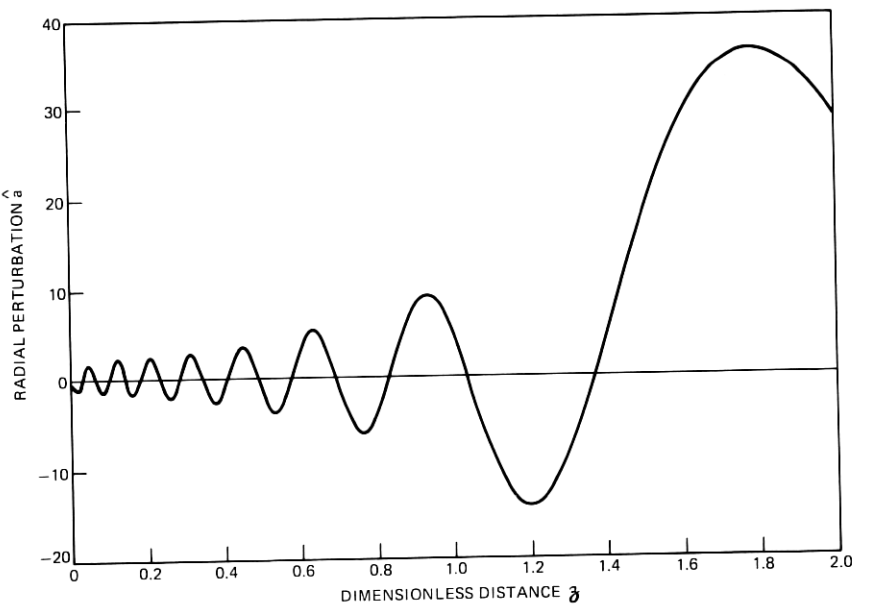

Fig. 8a—Surface perturbation for base state [eq. (22)] with $\omega = 100$, $\vartheta_L = 2$, at $T = 0$.

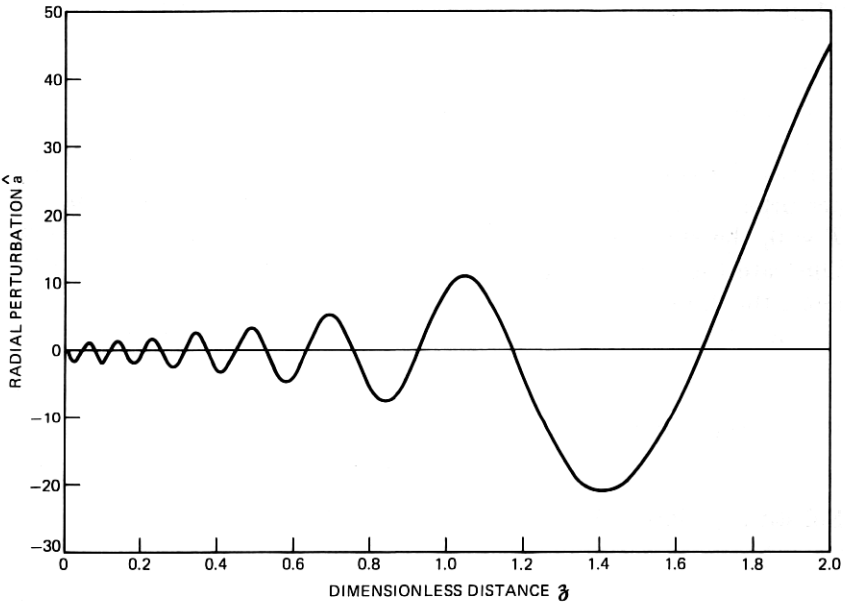

Fig. 8b—$\hat{a}$ at $T = 0.25$.

the compound space-time argument. If we substitute

$$\hat{a}' = h(\tau + \tfrac{1}{2}e^{-2\vartheta})e^{-2\vartheta},$$

this leads to $h = -\frac{1}{2}\dot{g}$; hence, the particular solution

$$\hat{a} = -\tfrac{1}{2}g(\tau + \tfrac{1}{2}e^{-2\vartheta}) = -\tfrac{1}{2}\hat{v}. \tag{56}$$

This suggests that any space-time history of viscosity changes given in the form (54) translates into changes of fiber radius by the factor $-\frac{1}{2}$. It is a traveling-wave type of response only in the sense that it is convected with the moving fluid.*

To take a specific example, consider a periodic viscosity perturbation, as would be caused by misalignment of the rotating laser beam used in heating the preform,

$$\hat{v} = \sin \omega(\tau + \eta), \tag{57}$$

* The negative sign may appear surprising at first. One notes, however, from the continuity equation (33) written as

$$(e^{-2\vartheta}\partial/\partial\tau + \partial/\partial\vartheta)\hat{a} = -\tfrac{1}{2}\hat{v}',$$

that $\hat{a}$ of the form $g(\tau + \frac{1}{2}e^{-2\vartheta})$ leads to $\hat{v}' = 0$. This means that such a form of radial perturbation can travel with the flowing fiber without perturbing the local velocity. Further, if a constant draw force is to be maintained, the expression

$$P/\rho = \pi a^2 \nu v'$$

shows that, with v' unperturbed, an increase in ν requires a decrease in a of half this magnitude.

where $\eta = \frac{1}{2}e^{-2\vartheta}$, yielding the particular solution

$$\hat{a}_p = -\tfrac{1}{2}\sin\omega\tau\cos\omega\eta - \tfrac{1}{2}\cos\omega\tau\sin\omega\eta. \tag{58}$$

The boundary conditions to be satisfied with the help of (51) are then

$$\begin{aligned} \hat{v}(0,\tau) &= 0, \qquad \hat{v}(\vartheta_L,\tau) = 0, \\ \hat{a}_c(0,\tau) &= \tfrac{1}{2}\sin\omega(\tau+\tfrac{1}{2}). \end{aligned} \tag{59}$$

In this case, the perturbations are driven only by the variations in viscosity.

An appropriate form for f is

$$f(\vartheta,\tau) = f_1\cos\omega(\tau+\eta) - f_2\sin\omega(\tau+\eta) \tag{60}$$

so that

$$\begin{aligned} \hat{a}_c(\vartheta,\tau) = {} & \tfrac{1}{2}(f_1\cos\omega\tau - f_2\sin\omega\tau)[Ci]_{\omega\eta}^{\omega/2} \\ & - \tfrac{1}{2}(f_1\sin\omega\tau + f_2\cos\omega\tau)[Si]_{\omega\eta}^{\omega/2} + \Phi(\tau), \end{aligned} \tag{61}$$

where

$$[Ci]_{\omega\eta}^{\omega/2} = \int_{\omega\eta}^{\omega/2}\frac{\cos w}{w}\,dw$$

$$[Si]_{\omega\eta}^{\omega/2} = \int_{\omega\eta}^{\omega/2}\frac{\sin w}{w}\,dw$$

and f_1, f_2 are integration constants. After determining $\Phi(\tau)$, f_1, and f_2 to satisfy (59), once again a solution of the form (52) is obtained, where A_1 and A_2 are recorded in Appendix D. It is interesting to note that $A(\omega,\vartheta_L)$ for this case, if normalized in terms of $\hat{v}_0$ and plotted as in Fig. 7 shows exactly the same response spectrum, but with half the amplitudes. Moreover, the profiles of radial perturbations along the fiber for this case strongly resemble the ones obtained for radial excitation at $\vartheta = 0$ (Fig. 8).

The sharp response peaks given by the above solutions at certain frequencies reflect the absence of quenching in the base flow (22). In search of some allowance for quenching effects, we consider two ad hoc modifications of the tensile fiber model: the base flow (25), which includes moderate quenching together with moderate draw-down, and base flow (23), which represents quenched, inertia-dominated, exponential draw-down.

Using eq. (78), which is based on (25), a solution of this perturbation equation is developed in Appendix D for the case of cyclic perturbations in the starting radius $\hat{a}(0,\tau) = \sin\omega\tau$. The resulting expression for $\hat{a}(\zeta,\tau)$ is recorded in (88). It turns out that the term $e^{-\gamma\zeta}\sin\omega\tau$ exceeds all other contributions to the dynamic response by several orders of magnitude for all values of ω and γ of interest. Thus, the perturbation in the fiber radius is merely a shift in the exponential

draw-down profile of the base state, whose spatial variation is independent of ω and characterized by γ, the quenching parameter of the base-flow viscosity profile $\nu = \nu_0 e^{\gamma\zeta}$. This perturbation oscillates in time with constant phase along the entire draw path. Typical profiles of $\hat{a}$ are shown in Fig. 9, again for $T = 0$, the start of a period, and $T = 0.25$, its quarter-point. A contribution from the nonexponential components in $\hat{a}(\zeta, \tau)$ is only seen at $T = 0$, the zero-crossing of its sin $\omega\tau$ term. These profiles show none of the spatial amplification evident in Fig. 8, which confirms, at least qualitatively, the attenuating effect of the quenching process. Unfortunately, a limiting comparison between the two models is not possible as the quenching effect is made to vanish, since that also requires a vanishing of the draw-down in base state (25).

If the quenched, inertia-dominated base flow (23) is employed in the inertialess perturbation equation (30), the resulting model is indeed subject to criticism as logically inconsistent. However, as a plausibility argument, we might suggest that inclusion of inertia in the base flow would at least give a qualitative indication of changes to be expected from a more complete allowance for inertia effects. The formal exercise, starting from (23) and (30), closely resembles the derivation of (79).

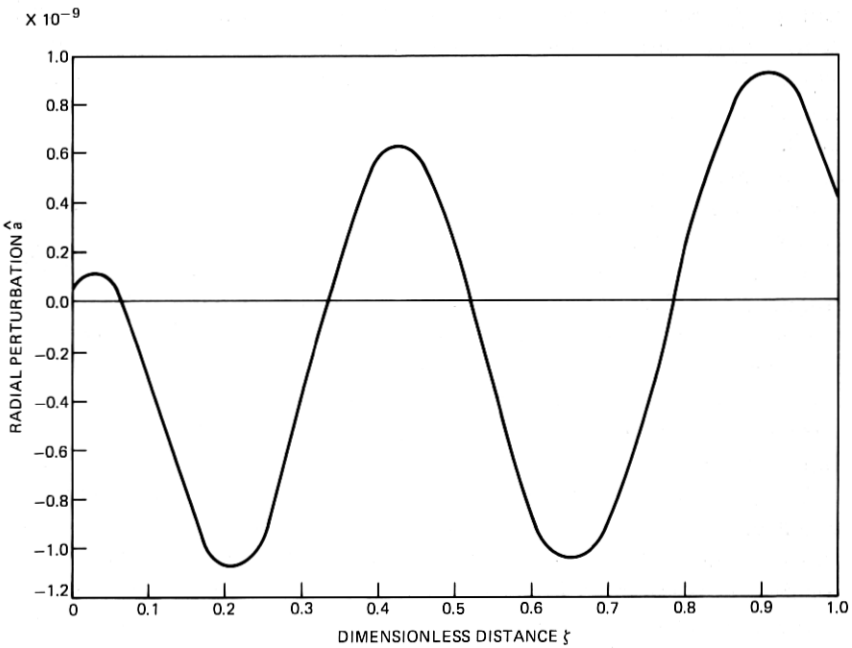

Fig. 9a—Surface perturbation for base state [eq. (25)] with $g = 0.75$, $\omega = 20$, $\gamma = 2$, at $T = 0$.

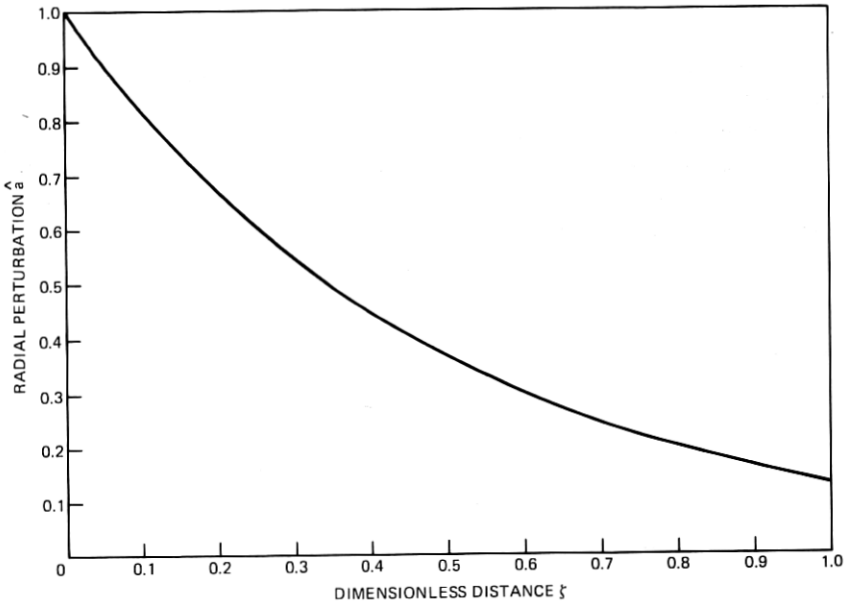

Fig. 9b—$\hat{a}$ at $T = 0.25$.

The resulting frequency response functions evolve quite clearly from curves such as Fig. 7 with considerable smoothing of peaks and valleys. This suppression of the response peaks, due to quenching, certainly agrees with experimental evidence.

The main point to be made in this preliminary assessment of tensile fiber models is that their frequency response curves and surface perturbation profiles bear little resemblance to the perturbations caused by surface tension, which we discuss in the next section. To generate more realistic response predictions for tensile fiber models, including inertia effects and heat transfer, we will have to resort to numerical means.

VIII. THE DYNAMIC RESPONSE OF CAPILLARY FIBER MODELS

We next inquire under what circumstances the well-known phenomena of surface-tension-driven perturbations on liquid filaments apply in the fiber-drawing problem. Indeed, there may be limited portions of the draw path, presumably near the hot tip of the forming zone, where the viscosity drops low enough for surface tension to become significant. At least for low-melting glasses, such as soda lime, this is a possibility, as born out by the comparison of essential terms in the base-flow equations of Section IV. We shall characterize this type of fluid-dynamic behavior as capillary fiber models. As we shall see,

their spatial response profiles under harmonic radial excitation are totally different from those of tensile fiber models. By all indications, these two kinds of filament response are fundamentally distinct phenomena. The ultimate question is to what extent they coexist and interact in a real fiber-drawing process.

Rayleigh's classical theory of capillary jets is our point of departure.[15,16] It shows that the growth rate of "varicose" perturbations (axisymmetric harmonic surface modulations) is given by

$$m = \frac{\sigma(\tilde{k}^2 - 1)}{2\mu a[\tilde{k}^2 + 1 - \tilde{k}^2 I_0^2(\tilde{k}) I_1^2(\tilde{k})]}, \tag{62}$$

where

m = real, the rate of growth
a = fiber radius
λ = wavelength of the perturbation
$\tilde{k} = 2\pi a/\lambda$
I_0 and I_1 = modified Bessel functions.

The denominator of (62) turns out to be negative for all $\tilde{k}$.*

If this capillary response model is locally applied to a base-flow model such as (24), assuming that base-state parameters change negligibly over the wavelength λ, we may use it to construct the dynamic response along a contracting fiber. Then the evolution of a small surface disturbance may be synthesized using the stepwise relation between displacement amplitudes at successive instants of time

$$U_{n+1} = U_n \left(\frac{a_{n+1}}{a_n} + \bar{m}\Delta t \right), \tag{63}$$

where

U_n and U_{n+1} = peak amplitudes of sinusoidal surface perturbations at t_n and t_{n+1}, respectively
$\frac{a_{n+1}}{a_n}$ = stepwise scale factor due to fiber draw-down
$\bar{m}$ = m at center of wavelength
$\Delta t = t_{n+1} - t_n$.

Our response simulation convects the end points of a given perturbative wavelength at their respective speeds, while computing local fiber

* Note that (62) results from a simplification of the characteristic equation, neglecting inertia effects, which in turn precludes initial conditions on perturbative velocities. However, it can be shown that the quantitative effect of this approximation on m is trivial (Ref. 19).

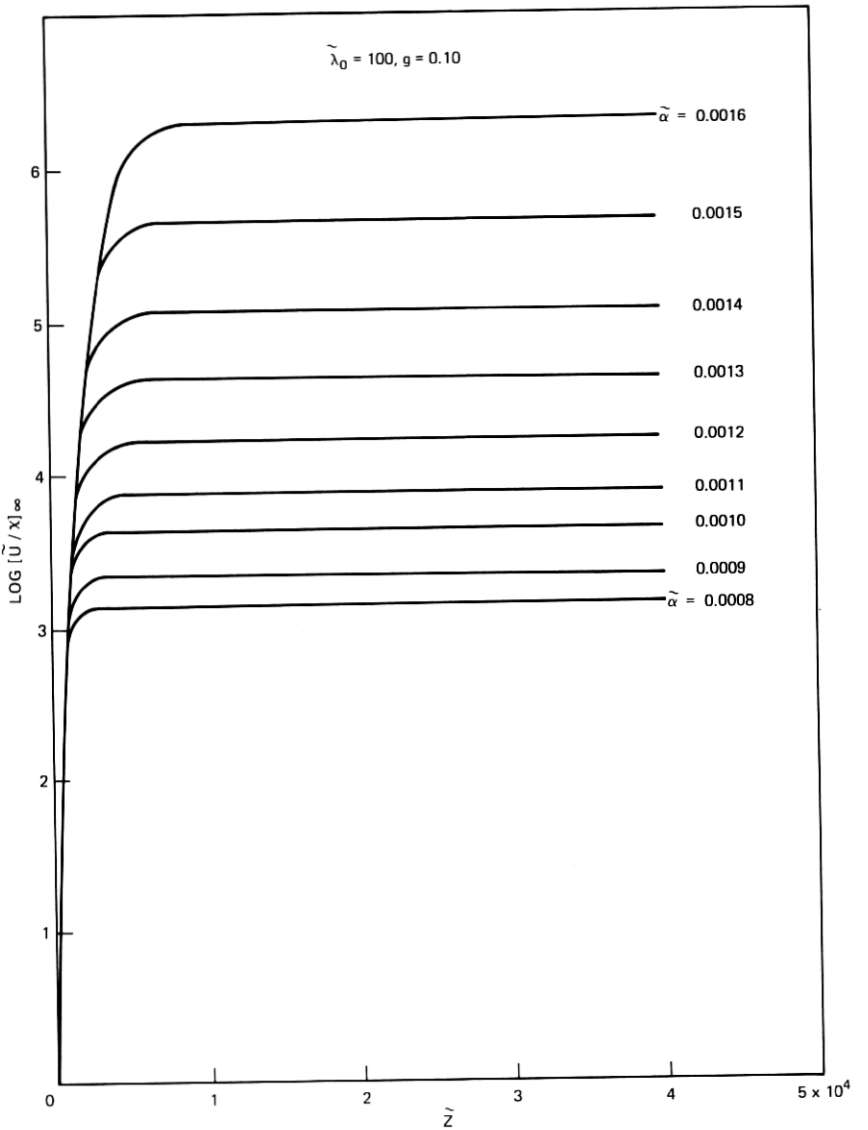

Fig. 10—Response histories for different values of $\tilde{\alpha}$.

properties from the base model (24). We use the notation:

$$\chi = a/a_0 \qquad \Psi = v/v_0 \qquad \eta = \mu/\mu_0$$
$$\tilde{U} = U/U_0, \qquad \tilde{\alpha} = \alpha a_0, \qquad \tilde{\lambda}_0 = \lambda_0/a_0,$$

and

$$\tilde{z} = (s + q)/2a_0,$$

where s, q, are end points of the perturbative wavelength. The nondimensionalized surface tension is assumed to vary as

$$\tilde{\sigma} = \tilde{\sigma}_0 e^{\tilde{\beta}\tilde{\alpha}\tilde{z}},$$

allowing for possible changes along the fiber (small values of $\tilde{\beta}$ approximate a linear dependence).

Figure 10 shows a set of response histories in terms of $\log [\tilde{U}/\chi]$ for $g = 0.1$, $\tilde{\lambda}_0 = 100$, $\tilde{\sigma}_0 = 0.25$, $\tilde{\beta} = 0$, $\eta_0 = 300$, and $0.0008 \leqq \tilde{\alpha} \leqq 0.0016$, illustrating the build-up to different asymptotic levels as a function of $\tilde{\alpha}$.

Figure 11 shows typical profiles of surface perturbations along the fiber for $\tilde{\lambda}_0 = 15.7$, which corresponds to a frequency of 200 Hz. As expected, the varicose response consists of sinusoids whose wavelength is progressively stretched due to fiber draw-down and whose amplitudes are modulated according to a response history such as given in Fig. 10. Note that this behavior differs drastically from the tensile fiber response of Figs. 8 and 9, which are also driven by radial harmonic excitation at the origin.

Figure 12 displays asymptotic response amplitudes for a range of initial wave numbers $2\pi/\tilde{\lambda}_0$ and several values of g, the terminal radius in units of a_0 for the base flow. For fixed g and $\tilde{\alpha}$, the response has a maximum in the neighborhood of $\tilde{\lambda}_0 = 50$. The low responses at short wavelengths are due to vanishing of the Rayleigh instability as $\tilde{\lambda}_0 \to 2\pi$

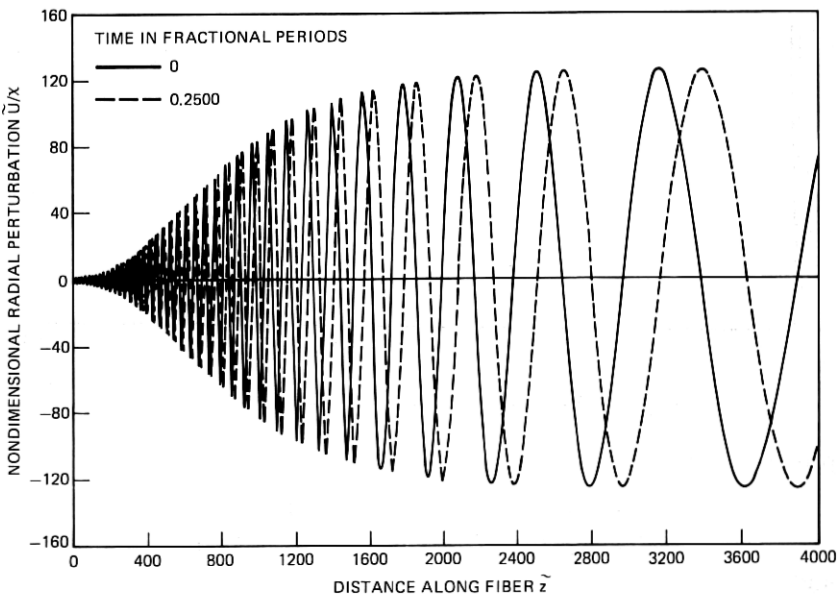

Fig. 11—Plot of deflected surface shapes for $\tilde{\lambda}_0 = 15.7$.

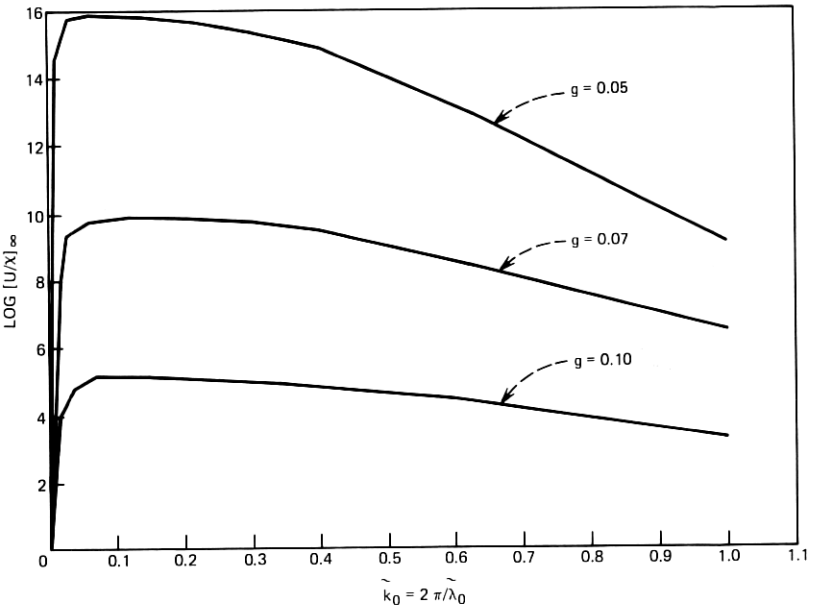

Fig. 12—Amplification factor vs dimensionless wave number for $\tilde{\alpha} = 0.001$.

while for large $\tilde{\lambda}_0$, hence large $\tilde{z}_0$, the perturbations encounter a rapid viscosity build-up along the fiber. Contrast these response curves with the ones for tensile models, and a fundamental difference is again apparent.

The influence of the terminal radius g, is illustrated in Fig. 13. As expected with a in the denominator of (62), increased draw-down (decreasing g) will enhance terminal perturbations. The second curve on that figure indicates the effect of $\tilde{\beta}$, the growth rate of surface tension. Finally Fig. 14 shows the decrease in response with initial viscosity, η_0 and the increase with rising values of $\tilde{\sigma}_0$, the initial surface tension.

Since the above simulation averages fiber properties over a perturbative wavelength and does not ensure continuity of perturbative surface velocities between time steps, it seemed appropriate to corroborate it by a slightly different model, due to Tomotika,[17,18] which is also germane to our situation. In Tomotika's study, filament contraction is effected by a surrounding medium subjected to extensional shear flow, as in some of Taylor's experiments.[9] This apparent difference in base flow and the need to let ambient viscosity approach zero for our purposes seems to limit the applicability of Tomotika's model to the fiber-drawing problem. However, as we shall see, it agrees quite well with our adaptation of Rayleigh's theory.

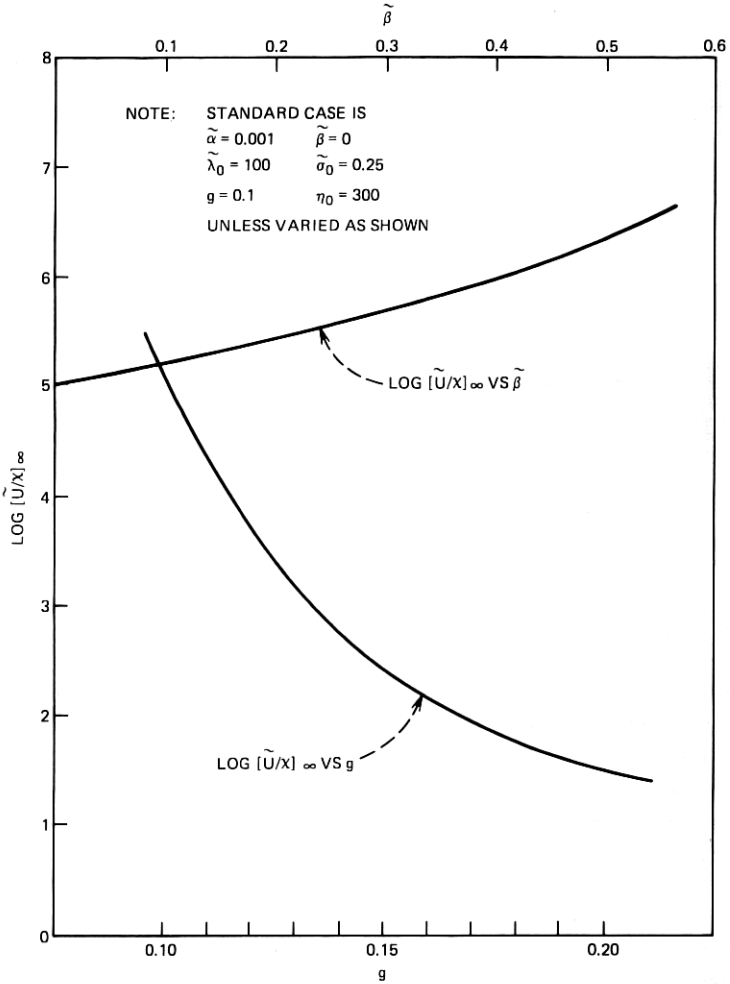

Fig. 13—Amplification factor vs g and $\tilde{\beta}$.

Tomotika finds the following asymptotic expression for interface perturbations as a function of several model parameters:

$$\log [\tilde{U}/\chi]_\infty = \tilde{\sigma}\xi\tilde{k}_0^{\frac{1}{2}} \int_0^{\tilde{k}_0} \psi(\tilde{k})d\tilde{k}, \tag{64}$$

where

ξ = ratio of filament to ambient viscosity
$\tilde{k} = 2\pi a/\lambda$ = local wave number of the perturbation
$\tilde{\sigma}$ = nondimensionalized surface tension
$\psi(\tilde{k})$ = a kernel that is detailed in the references.

The behavior of this expression is illustrated in Fig. 15 by plotting it against $\tilde{k}_0$ for various values of ξ. These plots show that, in the absence of quenching, the stabilizing effect of ambient shear flow diminishes steadily with ambient viscosity while the maximum response shifts to higher frequencies. This behavior is altered significantly if exponential changes of filament viscosity and surface tension are introduced to represent quenching effects, similar to our modification of Rayleigh's analysis. Equation (64) then changes to

$$\log [\tilde{U}/\chi]_\infty = \frac{\tilde{\sigma}_0}{3g^2\tilde{k}_0} \int_{g^2\tilde{k}_0}^{\tilde{k}_0} y(1 - \tilde{k}^2)\varphi(\tilde{k})d\tilde{k}, \qquad (65)$$

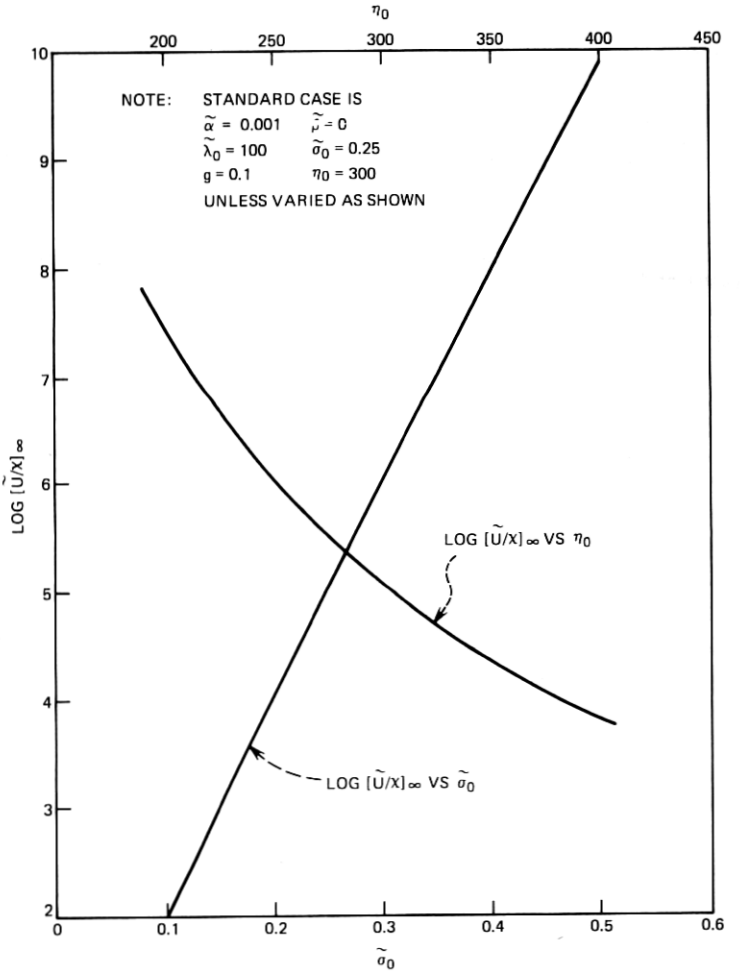

Fig. 14—Amplification factor vs η_0 and $\tilde{\sigma}_0$.

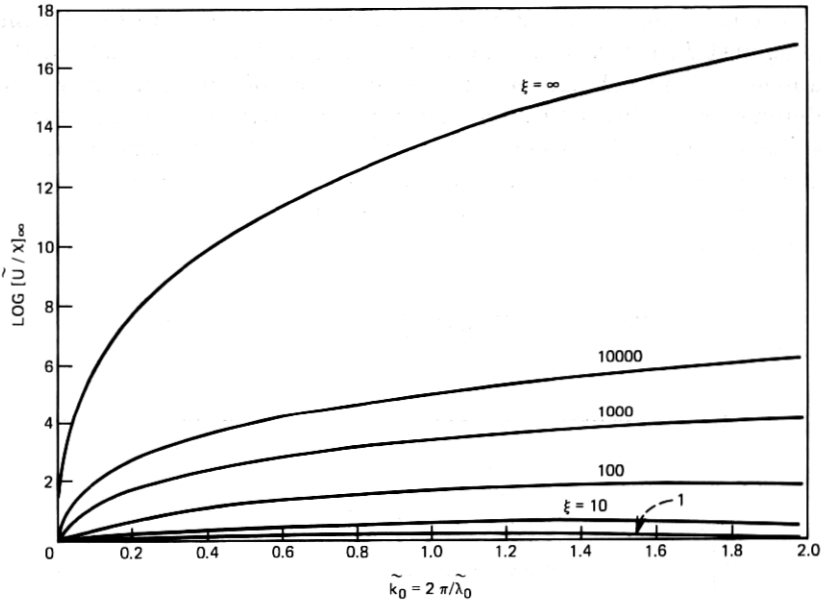

Fig. 15—Amplification factor vs $\tilde{k}_0$ for $\xi \to \infty$ (Tomotika's model with constant viscosity and surface tension).

where

$$y = e^{\tilde{\beta}\tilde{\alpha}\tilde{z}} = (1 - g)^{\tilde{\beta}} \left[\left(\frac{\tilde{k}}{\tilde{k}_0} \right)^{\frac{1}{2}} - g \right]^{-\tilde{\beta}}$$

and $\varphi(\tilde{k})$ is another kernel detailed in the references. Plots of this expression in Fig. 16 show good agreement with Fig. 12 for large ξ (and $g = 0.1$). Plots of (65) for $\xi = 10^6$ and various values of the terminal base flow radius are given in Fig. 17. They show the same response of $[\tilde{U}/\chi]_\infty$ for $g \to 0$ as Fig. 13.

In summary, these results indicate that the two capillary models of quenched fiber responses, obtained by modifying Rayleigh's and Tomotika's analyses, are essentially equivalent. Note again that none of the response curves, such as Fig. 17, bear any resemblance to those of tensile fiber models.

An additional piece of insight into capillary response mechanisms comes from Weber's work.[19] He reproduces Rayleigh's analysis by a somewhat different approach and obtains an exact equation for m, as well as a simplified expression that agrees with (62). Weber shows that the small errors in (62) are essentially due to the neglect of radial components of the flow field. He demonstrates this conclusively by rederiving (62) from a one-dimensional representation (recorded in Appendix E) which captures all salient features of the capillary re-

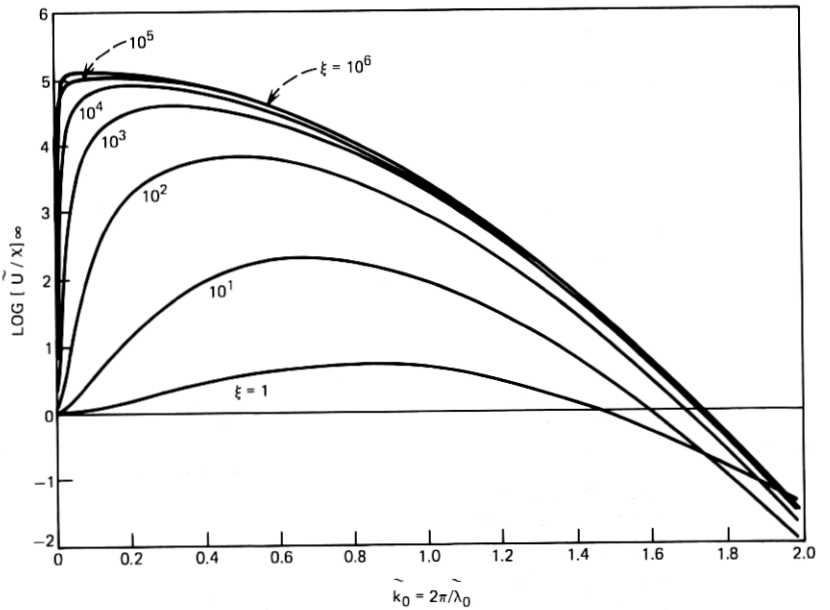

Fig. 16—Amplification factor vs $\tilde{k}_0$ for $\alpha = 0.001$, $g = 0.1$, and $1 \leqq \xi \leqq 10^6$ (modification of Tomotika's analysis for quenched base state).

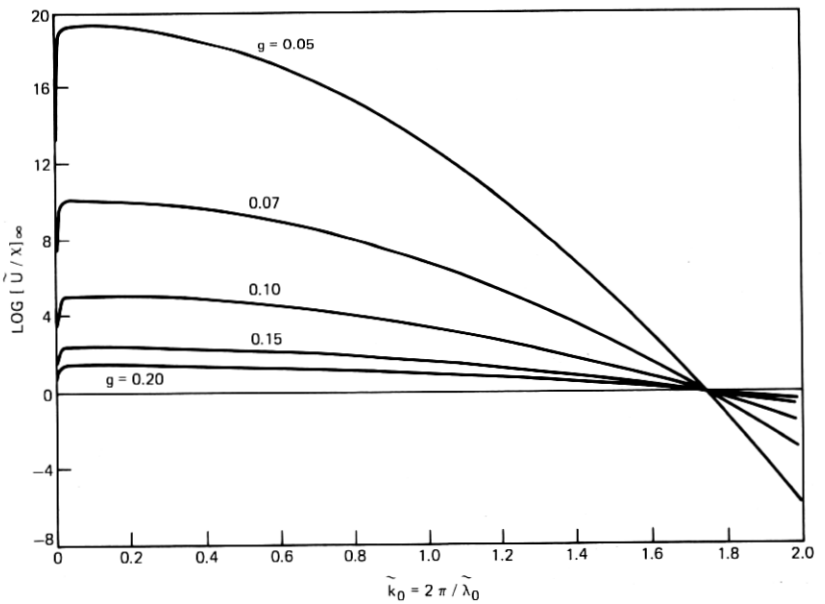

Fig. 17—Amplification factor vs $\tilde{k}_0$ for $\tilde{\alpha} = 0.001$, $\xi = 10^6$, and $0.005 \leqq g \leqq 0.20$ (modification of Tomotika's analysis for quenched base state).

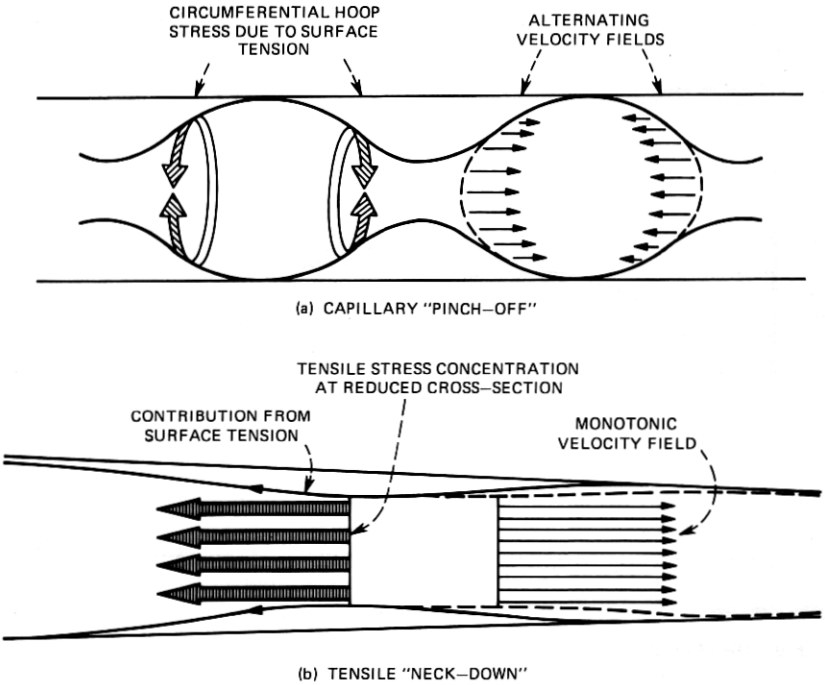

Fig. 18—Comparison of capillary and tensile instabilities.

sponse mechanism. Thus, multidimensionality is not the criterion that distinguishes capillary from tensile response models. The fundamental difference seems rather to lie in the energy source from which the perturbations are fed: surface tension in one case and axial stress in the other.

Figure 18 attempts to emphasize this distinction in a pictorial fashion: (*i*) In the capillary model, surface tension, by overcoming viscous stresses, tends to accumulate fluid from both directions into periodic "beads," ultimately pinching off individual droplets as the minimum energy configuration. A multiplicity of such separations can occur independently of each other, and the essential physical mechanism is equally as valid for stationary, uniform filaments as it is for contracting base flows. (*ii*) In the tensile model, on the other hand, the "worst" among random localized constrictions, due to surface perturbations, causes a tensile stress concentration which further reduces the cross-sectional area and results in a single, "run-away" tensile separation. This is the familiar necking of any tensile test specimen. The tensile stress associated with draw-down in the base flow is an essential prerequisite for this mechanism. Surface tension

will indeed contribute to tensile resistance in the necked down section, but it does not fundamentally alter the separation process.

Thus, the capillary mechanism is a contest between surface tension and viscosity, independent of filament draw-down, whereas in the tensile mechanism the viscous stresses, jointly with surface tension, attempt to resist the draw force.

IX. SUMMARY AND CONCLUSIONS

Several important observations result from the discussions in the preceding sections.

(*i*) Optical fiber drawing differs from textile fiber "spinning" in several essential ways. The flow of glass in the forming zone and draw-down region is dominated by viscous stresses. Inertia and surface tension play secondary roles. (They become noticeable only for the lower-melting glasses and then only in limited portions of the flow field.) This contrasts with polymer fiber forming, where, in some instances, viscosities can be quite low and other effects may be of comparable importance. Moreover, glass fibers are quenched over a wider range of temperatures than polymer fibers. This, together with the extreme temperature-dependence of glass viscosities, causes viscosity profiles along the draw path to rise much more abruptly than in textile fibers. Finally, and perhaps most importantly, molten glass can be considered very nearly Newtonian, which is not true for most polymers. Given the above physical features and the small-slope assumption of gradual draw-down, we can justify one-dimensional base states as useful representations of steady flow in the draw-down region.

(*ii*) Given a base-flow model, its sensitivity to changes in operating conditions, such as the take-up speed and temperature profile, can be estimated by first-order perturbations. It turns out that the draw-down profile is relatively insensitive to significant viscosity changes, assuming that interface conditions between the draw-down region and forming zone have been modeled correctly. For nontrivial forming zones, e.g., Fig. 1a, b, or d, it is difficult to make reasonable assumptions for these conditions. Since we lack a complete understanding of the forming zone, but expect its flow field to change with perturbations in the draw-down region, our results must be considered tentative.

(*iii*) Fundamental differences exist between the tensile and capillary models of dynamic fiber response. The tensile mechanism seems to prevail in most of the draw-down region. For low-melting

glasses, we conjecture that the capillary model may apply in the short and very hot transition between forming zone and draw-down region, where surface tension can sustain perturbations that subsequently propagate by the tensile mechanism. The interactions of these two phenomena and their relation to dynamic responses in the forming zone itself are presently not understood. In the following we amplify each of these points to some extent.

The base-flow models we supplied in Section IV are admittedly qualitative. A heat-transfer analysis was circumvented in this preliminary study by assuming exponential viscosity profiles, suggested by qualitative experimental evidence. Exact solutions of the coupled one-dimensional momentum and heat-transfer equations are now being carried out to allow for different kinds of heating in the forming zone and various cooling mechanisms in the draw-down region. The resulting simulation will be able to provide more detailed operational trade-offs between steady drawing parameters. It will also assess the limited influence of fluid inertia, surface tension, and gravity. Finally, this modeling effort presents a natural opportunity for experimental corroboration by suitably instrumented steady-state runs, using laser and/or furnace-heated preforms or crucibles.

As an extension of one-dimensional base-flow models, radial-heat-transfer mechanisms should be simulated, leading to nonuniform cross-sectional viscosity distributions at the start of the draw-down region. These viscosity distributions must be input to a perturbation model of axisymmetric free surface flow which generates the nonplanar velocity profiles expected in the transition between forming zone and draw-down region. Ultimately, the detailed flow fields of forming zones such as Fig. 1b and d may have to be simulated by discretization techniques. If properly combined, these efforts may, hopefully, result in a unified base-flow model that properly allows for interactions between the draw-down region and forming zone in representing steady-state responses to changes in the control parameters of the draw process.

Finally, as mentioned before, it appears that vastly different frequency response curves and longitudinal profiles of surface perturbations characterize tensile and capillary dynamic responses as fundamentally distinct physical mechanisms. (Note the intuitive distinctions given at the end of Section VIII.) They do not seem derivable, in proper relation, from some universal fiber stability analysis. The question is then, what must be done to develop them into parts of a realistic and unified dynamic response model.

Since analytic solutions for tensile responses of nontrivial base flows

in the draw-down region are not possible, numerical solutions by modal analysis or space-time integration are being attempted. This is expected to shed further light on the anti-intuitive response profiles obtained from the "inertialess" perturbation equations. Similarly, the capillary model applied so far to an elementary base flow may be implemented, by numerical means, for conditions representative of the transition between forming zone and draw-down region. Combining these extensions of the tensile and capillary response models, it may be possible to relate dynamic records of thermal or mechanical surface perturbations coming out of the forming zone to diameter variations in the finished fiber.

X. ACKNOWLEDGMENTS

I am indebted to Professor G. M. Homsy for numerous discussions of this study, to J. A. Lewis for detailed suggestions, and to P. G. Simpkins and E. Y. Harper for many helpful comments on this manuscript.

APPENDIX A

Implications of the Small-Slope Approximation

We briefly sketch the consequences of the small-slope approximation, $|a_z| \ll 1$ and $|u/v| \ll 1$, as they evolve from (1), (2), (3), and (4) by scaling arguments. Let

$$v = v_0\Psi, \quad u = u_0\varphi, \quad \mu = \mu_0\eta, \quad p = p_0\iota, \quad a = a_0\chi, \quad r = a_0\xi, \quad z = L\zeta, \quad \text{and} \quad t = \frac{L}{v_0}\tau. \tag{66}$$

Then the small-slope assumption amounts to

$$\left|\frac{u_0}{v_0}\right| = 0\left(\frac{a_0}{L}\right) = \epsilon \ll 1.$$

Substitution of (66) into (4) yields

$$\begin{aligned}
\tau_z &= \frac{\mu_0 v_0}{L}\left[-\frac{p_0 L}{\mu_0 v_0}\iota + 2\eta\Psi_\zeta\right] \doteq \frac{\mu_0 v_0}{L}\bar{\tau}_z \\
\tau_r &= \frac{\mu_0 v_0}{L}\left[-\frac{p_0 L}{\mu_0 v_0}\iota + 2\eta\varphi_\xi\right] \doteq \frac{\mu_0 v_0}{L}\bar{\tau}_r \\
\tau_\theta &= \frac{\mu_0 v_0}{L}\left[-\frac{p_0 L}{\mu_0 v_0}\iota + 2\eta\varphi/\xi\right] \doteq \frac{\mu_0 v_0}{L}\bar{\tau}_\theta \\
\tau_{rz} &= \frac{\mu_0 v_0}{L}\eta\left[\frac{1}{\epsilon}\Psi_\xi + \epsilon\varphi_\zeta\right] \doteq \frac{\mu_0 v_0}{L}\bar{\tau}_{rz},
\end{aligned} \tag{67}$$

where $p_0 L/\mu_0 v_0 = 0(1)$ and will be omitted henceforth. Substituting

(66) and (67) into (3),

$$\frac{\rho v_0 L}{\mu_0}\left[\Psi_\tau + \left(\frac{\mu_0 L}{v_0 a_0}\right)(\varphi\Psi_\xi + \Psi\Psi_\zeta)\right] = (-\iota + 2\eta\Psi_\zeta)_\zeta + \frac{1}{\epsilon^2}\frac{1}{\xi}[\xi\eta(\Psi_\xi + \epsilon^2\varphi_\zeta)]_\xi.$$

Considering the case $\rho v_0 L/\mu_0 = Re \ll 1$,

$$0 = \epsilon^2(-\iota + 2\eta\Psi_\zeta)_\zeta + \frac{1}{\xi}[\xi\eta(\Psi_\xi + \epsilon^2\varphi_\zeta)]_\xi.$$

Hence,

$$(\xi\eta\Psi_\xi)_\xi = 0.$$

If no constraint is to be imposed on η, we have

$$\Psi_\xi = 0 \tag{68}$$

and

$$\tau_{rz} = \frac{\mu_0 v_0}{L}\epsilon\eta\varphi_\zeta = 0[\epsilon(\tau_z, \tau_r, \tau_\theta)].$$

Now, from (1),

$$\Psi_\zeta + \left(\frac{\mu_0 L}{v_0 a_0}\right)(\varphi_\xi + \varphi/\xi) = 0$$

and because of (68)

$$\varphi_\xi = \varphi/\xi = -\tfrac{1}{2}\Psi_\zeta. \tag{69}$$

Then,

$$\bar{\tau}_r = \bar{\tau}_\theta = -\iota - \eta\Psi_\zeta \tag{70a}$$

$$\bar{\tau}_{rz} = -\frac{\epsilon}{2}\eta\xi\Psi_{\zeta\zeta}$$

and

$$\bar{\tau}_z = -\iota + 2\eta\Psi_\zeta. \tag{70b}$$

ι is determined from the normal stress condition at the fiber surface $\xi = \chi$. In dimensional form,

$$\tau_r + a_z^2\tau_z - 2a_z\tau_{rz} = \frac{\sigma(aa_{zz} - a_z^2 - 1)}{a(1 + a_z^2)^{\frac{1}{2}}}. \tag{71}$$

Substituting (66) and (70) into (71) and dropping terms of $0(\epsilon^2)$ and higher, as well as a_{zz}, one finds

$$\iota = \frac{\tilde{\sigma}}{\chi} - \eta\Psi_\zeta \tag{72}$$

for all values of ξ, where $\tilde{\sigma} = \sigma L/\mu_0 v_0 a_0$. With this result, $\bar{\tau}_z$ from (70a) becomes

$$\bar{\tau}_z = -\frac{\tilde{\sigma}}{\chi} + 3\eta\Psi_\zeta, \tag{73}$$

where 3η constitutes the "Trouton" viscosity. (The additional $\eta\Psi_\zeta$

term, augmenting $2\eta\Psi_\zeta$ in (70), originated in $\bar{\tau}_r$ of (71). This, in turn, is due to φ_ξ of (67), the cross-sectional contraction that necessarily accompanies the extensional flow of fiber drawing.) We also note from (72) and (70) that

$$(\iota + \eta\Psi_\zeta)_\xi = \tau_{r_\xi} = \tau_{\theta_\xi} = 0, \tag{74}$$

which agrees with the radial equilibrium equation if (66), (68), and (70) are used in (2) and we let $Re \ll 1$.

The tangential surface stress condition at $\xi = \chi$ reads

$$a_z(\tau_r - \tau_z) + (1 + a_z^2)\tau_{rz} = 0 \tag{75}$$

and, if rendered dimensionless, has leading terms of $0(\epsilon)$; hence, it will be ignored. For completeness, we also note that the kinematic boundary condition (7), rendered dimensionless and time-invariant, yields

$$\frac{\Psi_\zeta}{\Psi} = -\frac{2\chi_\zeta}{\chi},$$

which is the time-invariant continuity equation (9).

APPENDIX B

Second-Order Perturbation Term for the Base-Flow Solution [Eq. (17)]

$$\begin{aligned}
\mathcal{K}[a, b, c, d, \zeta] = {} & \zeta\left(1 + \frac{ab^2}{2} + d + \frac{d^2}{2} + \frac{d^3}{6}\right) + \frac{\zeta_c^2}{2}\left(1 + d + \frac{d^2}{2}\right) \\
& + \frac{\zeta^3 c^2}{6}(1 + d) + \frac{\zeta^4 c^3}{24} \\
& + \frac{1}{lnE}\left[\left(1 + d + \frac{d^2}{2}\right)(ae^{\zeta lnE} - 2be^{-(lnE/2)\zeta}) \right. \\
& + (1 + d)\left(\frac{a^2}{4}e^{2\zeta lnE} + 2abe^{(lnE/2)\zeta} - \frac{b^2}{2}e^{-\zeta lnE}\right) \\
& \left. + \frac{a^3}{18}e^{3\zeta lnE} + \frac{a^2 b}{3}e^{(3lnE/2)\zeta} - \frac{b^3}{9}e^{-(3lnE/2)\zeta}\right] \\
& - \frac{11}{lnE}\left[(a - 2b)\left(1 + d + \frac{d^2}{2}\right)\right. \\
& \left. + \left(\frac{a^2}{4} + 2ab - \frac{b^2}{2}\right)(1 + d) + \frac{a^3}{18} + \frac{a^2 b}{3} + \frac{b^3}{9}\right] \\
& + c\left\{(1 + d)\left[aF(lnE, \zeta) + bF\left(-\frac{lnE}{2}, \zeta\right)\right]\right. \\
& + \frac{a^2}{2}F(2lnE, \zeta) + abF\left(\frac{lnE}{2}, \zeta\right) + \frac{b^2}{2}F(-lnE, \zeta) \\
& \left. + \frac{c^2}{2}\left[aG(lnE, \zeta) + bG\left(-\frac{lnE}{2}, \zeta\right)\right]\right\},
\end{aligned}$$

where

$$F(\gamma, \zeta) = \frac{1}{\gamma}\left[(\zeta - \gamma)e^{\gamma\zeta} + \frac{1}{\gamma}\right]$$

and

$$G(\gamma, \zeta) = \frac{1}{\gamma}\left[\left(\zeta^2 + \frac{2\zeta}{\gamma} + \frac{2}{\gamma^2}\right)e^{\gamma\zeta} - \frac{2}{\gamma^2}\right].$$

APPENDIX C

Differential Equations for First-Order Dynamic Perturbations in the Radius, $\hat{a}$

Using (33) to eliminate $\hat{v}$ from the first-order variations of the momentum equations, we obtain from (35), which reflects the quenched, inertia-dominated base state (23) with inertia effects in the perturbation equation,

$$\hat{a}'''' + \hat{a}\cdot''' e^{-2\vartheta} + 2\hat{a}''' - 4\hat{a}\cdot'' e^{-2\vartheta} - 2\hat{a}\cdot\cdot e^{-4\vartheta} + 8\hat{a}\cdot\cdot e^{-4\vartheta} - 4\hat{a}'' - 8\hat{a}' = 4\hat{p}' + 4\hat{p}'' + \hat{p}'''. \quad (76)$$

From (34), the inertialess momentum equation, and the unquenched, inertialess base state (22), we obtain

$$\hat{a}'' + \hat{a}\cdot' e^{-2\vartheta} = \hat{p}'. \quad (77)$$

Note in (76) and (77) that $(\ )' = \partial(\ )/\partial\vartheta$ and $(\ )\cdot = \partial(\ )/\partial\tau$, where $\vartheta = \alpha z/L$ and $\tau = \alpha v_0 t/L$. Finally, from (28) and (30), the inertialess momentum equation with the quenched inertialess base state (25), we can find

$$\left(\frac{\partial}{\partial\zeta} + \frac{1}{\psi}\frac{\partial}{\partial\tau}\right)(\hat{a}' + \alpha\hat{a}) = \frac{e^{-\alpha\zeta}}{2}\hat{p}', \quad (78)$$

where $\psi = v/v_0$ as in (25), $\zeta = z/L$ and $\tau = tv_0/L$. In this case, $(\ )' = \partial(\ )/\partial\zeta$.

APPENDIX D

Detailed Results for Forced Dynamic Responses of the Tensile Fiber Model

The detailed expressions for A_1 and A_2 resulting from (58) and (61) are

$$A_1 = \left\{\frac{1}{2}[\cos]_{\omega\eta}^{\omega/2} + \frac{(1-\epsilon)\omega}{4\epsilon(B_1^2 + B_2^2)} \times [(-B_1 \sin\omega/2 + B_2\cos\omega/2) \times [Ci]_{\omega/2\epsilon}^{\omega/2} - (B_1\cos\omega/2 + B_2\sin\omega/2) \times [Si]_{\omega/2\epsilon}^{\omega/2}]\right\}$$

$$A_2 = \left\{\frac{1}{2}[\sin]_{\omega\eta}^{\omega/2} + \frac{(1-\epsilon)}{4\epsilon(B_1^2 + B_2^2)} \times [(B_1\cos\omega/2 + B_2\sin\omega/2) \times [Ci]_{\omega/2\epsilon}^{\omega/2} + (-B_1\sin\omega/2 + B_2\cos\omega/2) \times [Si]_{\omega/2\epsilon}^{\omega/2}]\right\},$$

where $\epsilon = e^{2\vartheta_L}$ and

$$B_1 = \left[Ci + \frac{\omega}{2\epsilon} Si + \cos \right]_{\omega/2\epsilon}^{\omega/2}$$
$$B_2 = \left[Si - \frac{\omega}{2\epsilon} Ci + \sin \right]_{\omega/2\epsilon}^{\omega/2}. \tag{79}$$

Recall that $\vartheta = \alpha z/L$.

We now parallel the development of Section VII for the quenched base flow (25). Equation (78) with $\hat{p} \equiv 0$ suggests a solution of the form

$$\hat{a}(\zeta, \tau) = Re \left\{ f_0 \int_0^\zeta \exp[\alpha(\zeta' - \zeta)] \exp[i\omega(\tau - \xi)] d\zeta' + \Phi_0 \exp(i\omega\tau - \alpha\zeta) \right\},$$

where

$$\xi = \int_0^{\zeta'} \frac{d\zeta^*}{v(\zeta^*)}, \qquad f_0 = f_1 + if_2, \qquad \Phi_0 = \Phi_1 + i\Phi_2. \tag{80}$$

Explicitly,

$$\hat{a}(\zeta, \tau) = A_1 \sin \omega\tau + A_2 \cos \omega\tau,$$

where

$$A_1(\zeta) = \int_0^\zeta e^{\alpha(\zeta' - \zeta)} (f_1 \sin \omega\xi - f_2 \cos \omega\xi) d\zeta' - \Phi_2 e^{-\alpha\zeta},$$
$$A_2(\zeta) = \int_0^\zeta e^{\alpha(\zeta' - \zeta)} (f_1 \cos \omega\xi + f_2 \sin \omega\xi) d\zeta' + \Phi_1 e^{-\alpha\zeta}, \tag{81}$$

describing the ζ-dependent phase and amplitude of the response. Note that $\zeta = z/L$ and $\tau = tv_0/L$, whereas in (79) $\vartheta = \alpha\zeta$ and $\tau = \alpha v_0 t/L$.

We use the same boundary conditions as in developing (52). For cyclic radial perturbations at $\zeta = 0$,

$$\hat{a}(0, \tau) = \sin \omega\tau, \tag{82}$$

together with the velocity conditions

$$\hat{v}(0, \tau) \equiv 0 \qquad \hat{v}(1, \tau) \equiv 0.$$

An expression for $\hat{v}$ is obtained by eliminating $\hat{v}'$ from (28) and (30)

$$\hat{v} = \frac{2}{v'} \dot{\hat{a}} + \frac{2v}{v'} \hat{a}' - 2\hat{a} + 2G(\tau), \tag{83}$$

where $G(\tau)$ is an arbitrary time function and the differentiation symbols mean $(\ )^{\cdot} = \partial(\ )/d\tau$, $(\ )' = \partial(\ )/\partial\zeta$. Substituting (81) into (83) we find

$$\hat{v}(\zeta, \tau) = V_1 \sin \omega\tau + V_2 \cos \omega\tau$$

with

$$V_1(\zeta) = \frac{-2\omega}{\psi'}\int_0^\zeta e^{\alpha(\zeta'-\zeta)}(f_1\cos\omega\xi + f_2\sin\omega\xi)d\zeta'$$
$$- 2\int_0^\zeta e^{\alpha(\zeta'-\zeta)}(f_1\sin\omega\xi - f_2\cos\omega\xi)d\zeta'$$
$$+ 2e^{-\alpha\zeta}\left[\left(\frac{\psi}{\psi'}\alpha + 1\right)\Phi_2 - \frac{\omega}{\psi'}\Phi_1\right]$$
$$+ \frac{2\psi}{\psi'}(f_1\sin\omega\xi - f_2\cos\omega\xi) + 2G_1$$

$$V_2(\zeta) = \frac{2\omega}{\psi'}\int_0^\zeta e^{\alpha(\zeta'-\zeta)}(f_1\sin\omega\xi - f_2\cos\omega\xi)d\zeta'$$
$$- 2\int_0^\zeta e^{\alpha(\zeta'-\zeta)}(f_1\cos\omega\xi + f_2\sin\omega\xi)d\zeta'$$
$$- 2e^{-\alpha\zeta}\left[\frac{\omega}{\psi'}\Phi_2 + \left(\frac{\psi}{\psi'}\alpha + 1\right)\Phi_1\right]$$
$$+ \frac{2\psi}{\psi'}(f_1\cos\omega\xi + f_2\sin\omega\xi) + 2G_2. \quad (84)$$

Ultimately, (82) leads to

$$\Phi_1 = 0, \qquad \Phi_2 = -1$$
$$f_1 = (B_1C_1 + B_2C_2)/(B_1^2 + B_2^2) \qquad f_2 = (f_1B_2 - C_2)/B_1$$
$$G_1 = 1 + \frac{1}{\psi_0'}(\alpha + f_2\cos\omega\xi_0 - f_1\sin\omega\xi_0) \quad (85)$$
$$G_2 = -\frac{1}{\psi_0'}(\omega + f_1\cos\omega\xi_0 + f_2\sin\xi_0),$$

where

$$B_1 = \frac{\omega}{\psi_1'}H(1) - K(1) + \frac{\psi_1}{\psi_1'}\cos\omega\xi_1 - 1$$
$$B_2 = -\frac{\omega}{\psi_1'}K(1) - H(1) + \frac{\psi_1}{\psi_1'}\sin\omega\xi_1 \quad (86)$$
$$C_1 = \frac{\omega}{\psi_0'} - \frac{\omega}{\psi_1'}e^{-\alpha}$$
$$C_2 = \left(\frac{\psi_1}{\psi_1'}\alpha + 1\right)e^{-\alpha} - \frac{\alpha}{\psi_0'} - 1.$$

The subscripts 0, 1 denote evaluation at $\zeta = 0, 1$ respectively, and the quantities H, K are defined as

$$H(\zeta) = \int_0^\zeta e^{\alpha(\zeta'-\zeta)}\sin\omega\xi d\zeta'$$
$$K(\zeta) = \int_0^\zeta e^{\alpha(\zeta'-\zeta)}\cos\omega\xi d\zeta'. \quad (87)$$

With this notation, we ultimately get

$$\hat{a}(\zeta, \tau) = [f_1 H(\zeta) - f_2 K(\zeta) + e^{-\alpha \zeta}] \sin \omega\tau + [f_1 K(\zeta) + f_2 H(\zeta)] \cos \omega\tau. \quad (88)$$

APPENDIX E

Weber's Derivation of the Capillary Stability Equation

This appendix gives a simplified derivation of the stability equation for the capillary fiber model based on assumptions that are quite equivalent to those made for the one-dimensional tensile model. In fact, the rationale used here closely parallels that of Section III.

The analysis proceeds in terms of equilibrium and continuity equations, which we write in dimensional form for the entire filament cross-section. The perturbed surface radius becomes $a + \delta$ and a given cross-sectional element is displaced by vdt along the fiber over the time increment dt. The radius of this element now becomes

$$a + \delta + \frac{\partial \delta}{\partial t} dt + \frac{\partial \delta}{\partial z} vdt. \quad (89)$$

Since the last term is of higher order, it will be neglected.

The constitutive relations are as in (4) and the derivation of an expression for τ_z is quite similar to Appendix A. The main difference arises in the radial stress boundary condition, where, in distinction from the treatment of (72), the longitudinal curvature term cannot be neglected for varicose perturbations. Then the r.h.s. of (72) becomes

$$\sigma \left(\frac{\delta}{a^2} + \delta'' \right) \quad (90)$$

and, instead of (74),

$$\tau_z = \sigma \left(\frac{\delta}{a^2} + \delta'' \right) + 3\mu v'. \quad (91)$$

The continuity equation yields

$$\frac{2}{a} \dot{\delta} + v' = 0. \quad (92)$$

Now, combining (9) and (10),

$$\tau_z' = \rho \dot{v} + \rho v v', \quad (93)$$

where the last term was apparently overlooked by Weber but seems to have little effect on the resulting stability equation.

Substituting (91) and (92) into (93) and assuming surface perturbations of the form $\delta = \delta^* e^{mt} \cos kz/a$, leads to the stability equation

$$m^2 + m \frac{(3\mu)}{\rho a^2} \tilde{k}^2 = \frac{\sigma}{2\rho a^3} (1 - \tilde{k}^2) \tilde{k}^2. \quad (94)$$

The unstable root, of interest here, is

$$m = -\frac{(3\mu)\tilde{k}^2}{2\rho a^2} + \left[\frac{\sigma}{2\rho a^3}(1 - \tilde{k}^2)\tilde{k}^2 + \frac{(3\mu)^2\tilde{k}^4}{4\rho^2 a^4}\right]^{\frac{1}{2}}. \quad (95)$$

REFERENCES

1. A. Ziabicki and R. Takserman-Krozer, "Formation and Breakage of Liquid Threads: I. Mechanism," Rocz. Chem., Ann. Soc. Chim. Polonorum, *37* (1963), p. 1503.
2. Ibid.: V. Range of Occurrence of the Individual Break Processes: General Conclusions," *38* (1964), p. 653.
3. Ibid.: VI. Following the Break Process with High-Speed Photography," *38* (1964), p. 1221.
4. A. Ziabicki, "Principles of Melt Spinning," in *Man Made Fibers*, eds., H. F. Mark, S. M. Atlas, and E. Cernia, Interscience, 1967, pp. 169–240.
5. J. R. A. Pearson and M. A. Matovitch, "Spinning a Molten Threadline, Part I," Ind. and Eng. Chem. Fundamentals, *8* (1969), p. 512.
6. S. Kase and T. Matsuo, "Studies on Melt Spinning: I. Fundamental Equations on the Dynamics of Melt Spinning," J. Appl. Polym. Sci., Part A, *3* (1965), p. 2541.
7. Ibid.: II. Steady State and Transient Solutions of Fundamental Equations Compared With Experimental Results," J. Appl. Polym. Sci., *11* (1967), p. 251.
8. M. M. Denn and C. J. S. Petrie, "Instabilities in Polymer Processing," A. I. Ch. E. Journal, March 1976, p. 209.
9. G. I. Taylor, "The Formation of Emulsions in Definable Fields of Flow," Proc. Roy. Soc., Series A, *146* (1934), p. 501.
10. E. A. J. Marcatili, "What Kind of Optical Fiber for Long-Distance Transmission?," S.P.I.E. Journal, *8* (1970), p. 101.
11. S. S. Kutukov and M. D. Khodakovskii, "Investigating the Movement of Glass in the Forming of Continuous Glass Fiber by High Speed Filming," Inst. of Glass Fiber, translated from Steklo i Keramika, *21*, No. 2 (1964), pp. 3–10.
12. A. Ziabicki and R. Takserman-Krozer, "Formation and Breakage of Liquid Threads, II. Cohesive Break of a Steady Liquid Jet," Rocz. Chem., Ann. Soc. Chim. Polonorum, *37* (1963), p. 1511.
13. Ibid.: IV. Effect of Rheological Behavior on Length of Liquid Threads," *38* (1964), p. 465.
14. J. R. A. Pearson and M. A. Matovitch, "Spinning a Molten Threadline, Part II," Ind. and Eng. Chem. Fundamentals, *8* (1969), p. 605.
15. S. Chandrasekhar, *Hydrodynamic and Hydromagnetic Stability*, Oxford: Clarendon Press, 1961.
16. Lord Rayleigh, "On the Instability of a Cylinder of Viscous Liquid Under Capillary Force," Phil. Mag., *34* (1892), p. 145.
17. S. Tomotika, "On the Instability of a Cylindrical Thread of a Viscous Liquid Surrounded by Another Viscous Fluid," Proc. Roy. Soc., *A150* (1935), p. 322.
18. S. Tomotika, "Breaking up of a Drop of Viscous Liquid Immersed in Another Viscous Fluid Which is Extending at a Uniform Rate," Proc. Roy. Soc., *A153* (1936), p. 302.
19. C. Weber, "Zum Zerfall eines Flüssigkeitsstrahles," Zeitschrift f. ang. Math. und Mech., *11* (1931), p. 136.
20. A. Ziabicki and R. Takserman-Krozer, "Formation and Breakage of Liquid Threads, III. Capillary Break-up of a Steady Viscous Jet," Rocz. Chem. Ann. Soc. Chim. Polonorum, *37* (1963), p. 1607.
21. S. Kasé, "Studies on Melt Spinning: III. Velocity Field Within the Thread." J. Appl. Polym. Sci., *18* (1974), p. 3267.
22. Ibid.: IV. On the Stability of Melting Spinning." *18* (1974), p. 3279.
23. S. Krishnan and L. R. Glicksman, "A Two-Dimensional Analysis of a Heated Free Jet at Low Reynolds Numbers," J. of Basic Eng., *93*, No. 3 (1971), p. 355.
24. F. T. Geyling, "The Glass Fiber Drawing Process and Its Stability Characteristics," 14th International Congress of Theoretical and Applied Mechanics, Delft, Netherlands (1976).
25. G. J. Donnelly and C. B. Weinberger, "Stability of Isothermal Fiber Spinning of a Newtonian Fluid," Ind. and Eng. Chem. Fundamentals, *14* (1975), p. 334.